

# Global simulations of magnetorotational turbulence II: turbulent energetics

E. R. Parkin<sup>\*</sup>

*Research School of Astronomy and Astrophysics, Australian National University, Canberra, ACT 2611, Australia*

Accepted ... Received ...; in original form ...

## ABSTRACT

Magnetorotational turbulence draws its energy from gravity and ultimately releases it via dissipation. However, the quantitative details of this energy flow have not been assessed for global disk models. In this work we examine the energetics of a well-resolved, three-dimensional, global magnetohydrodynamic accretion disk simulation by evaluating statistically-averaged mean-field equations for magnetic, kinetic, and internal energy using simulation data. The results reveal that turbulent magnetic (kinetic) energy is primarily injected by the correlation between Maxwell (Reynolds) stresses and shear in the (almost Keplerian) mean flow, and removed by dissipation. This finding differs from previous work using local (shearing-box) models, which indicated that turbulent kinetic energy was primarily sourced from the magnetic energy reservoir. Lorentz forces provide the bridge between the magnetic and kinetic energy reservoirs, converting  $\sim 1/5$  of the total turbulent magnetic power input into turbulent kinetic energy. The turbulent energies (both magnetic and kinetic) are mainly driven by terms associated with the turbulent fields, with only a minor influence from mean magnetic fields. The interaction between mean and turbulent fields is most evident in the induction equation, with the mean radial magnetic field being strongly influenced by the turbulent electromotive force (EMF).

During the quasi-steady turbulent state roughly 2/3 of the Poynting flux travels into the corona, with the remainder transporting magnetic energy in the radial direction. In contrast to previous studies, the stress-related part of the Poynting flux is found to dominate, which may have important implications for “reflection” models of Seyfert galaxy coronae that typically invoke a picture of buoyant rising of magnetic flux tubes via advection.

**Key words:** accretion, accretion disks - MHD - instabilities - turbulence

## 1 INTRODUCTION

Accretion disks possessing a weak initial seed magnetic field, a radially decreasing angular velocity, and electrical conductivity are unstable to the magnetorotational instability (MRI - Balbus & Hawley 1991, 1998). Astrophysical disks, which typically have a Keplerian rotation profile, satisfy this requirement. Following the linear phase of instability growth, fully developed, self-sustaining turbulence establishes (Hawley et al. 1995; Brandenburg et al. 1995). The same turbulent stresses that provide energy injection simultaneously drive angular momentum transport, thus enabling the maintenance of the turbulence in tandem with ongoing accretion (Balbus & Hawley 1998).

Over the past two decades magnetorotational turbulence has taken central stage as the much sought angular mo-

mentum transport mechanism in accretion disks. However, transporting angular momentum is not the entire story. The very fact that the turbulence is self-sustaining raises questions about energetics. Primarily, what is the energy source, how (if at all) is energy removed from the disk, and what role does turbulence play? These questions have been broached previously but only using local (shearing-box) models of accretion disks (Brandenburg et al. 1995; Gardiner & Stone 2005b; Fromang & Papaloizou 2007; Simon et al. 2009). Recent work by Parkin & Bicknell (2013b) has highlighted important differences between local and global accretion disk models in terms of the influence of boundary conditions on both the mean field and magnetic energy evolution. This raises the question of whether or not the shearing-box approximation captures the physics of energy generation accurately. The establishment of an outer scale to the turbulence (i.e. a turn-over in the power spectra at low wavenumber) in the shearing-box simulations presented by Davis et al.

<sup>\*</sup> E-mail: ross.parkin@anu.edu.au

(2010) would suggest that the situation should not change considerably when moving to a global disk. Nevertheless, this intuition requires confirmation. With this in mind, in this work we examine the transport of energy using the results of a high resolution global accretion disk simulation coupled to a Reynolds averaged mean field analysis (e.g. Balbus & Hawley 1998; Kuncic & Bicknell 2004).

In common with previous work we find that shear-stress correlations are at the heart of the turbulent energy source, both for the magnetic and kinetic energies (Brandenburg et al. 1995). However, in contrast, we find that the turbulent kinetic energy gains the majority of its power from the hydrodynamic interaction between Reynolds stresses and mean flow shear, and is not primarily driven by Lorentz forces. Mean magnetic fields are not observed to directly influence the turbulent energies. However, a turbulent field is by definition a deviation from a mean field. The prominence of turbulent fields in driving mean field induction therefore highlights the mean-turbulent field interaction, which evidences the indirect nature by which mean magnetic fields influence turbulent energy evolution.

The remainder of this paper is organised as follows: in § 2 we describe the simulation setup and averaging procedures used in this investigation. In § 3 we present basic characteristics of the mean and turbulent fields in the disk. The results from the application of a control-volume analysis to the simulations are presented in § 4. We discuss the global energy flow and make a comparison with previous work in § 5, closing with conclusions in § 6.

## 2 THE MODEL

### 2.1 Simulation code

The time-dependent equations of ideal magnetohydrodynamics are solved using the PLUTO code (Mignone et al. 2007) in a 3D spherical  $(r, \theta, \phi)$  coordinate system. The relevant equations for mass, momentum, energy conservation, and magnetic field induction are:

$$\frac{\partial \rho}{\partial t} + \nabla \cdot (\rho \mathbf{v}) = \dot{M}_{\text{source}}, \quad (1)$$

$$\frac{\partial \rho \mathbf{v}}{\partial t} + \nabla \cdot (\rho \mathbf{v} \mathbf{v} - \mathbf{B} \mathbf{B}) + \nabla p = -\rho \nabla \Phi, \quad (2)$$

$$\frac{\partial E}{\partial t} + \nabla \cdot ((E + p_{\text{tot}}) \mathbf{v} - (\mathbf{v} \cdot \mathbf{B}) \mathbf{B}) = -\rho \mathbf{v} \cdot \nabla \Phi - \rho \Lambda \quad (3)$$

$$\frac{\partial \mathbf{B}}{\partial t} = \nabla \times (\mathbf{v} \times \mathbf{B}). \quad (4)$$

Here  $E = u_\epsilon + u_K + u_B$  is the total energy,  $u_\epsilon = \rho \epsilon$  is the internal energy,  $\epsilon$  is the specific internal energy,  $u_K = \frac{1}{2} \rho |\mathbf{v}|^2$  is the total kinetic energy,  $\mathbf{v}$  is the velocity,  $\rho$  is the mass density,  $p$  is the gas pressure,  $u_B = \frac{1}{2} |B|^2$  is the magnetic energy/pressure, and  $p_{\text{tot}} = p + u_B$  is the total (gas plus magnetic) pressure. We use an ideal gas equation of state,  $p = (\gamma - 1)u_\epsilon$ , with an adiabatic index  $\gamma = 5/3$ . The adopted scalings for density, velocity, temperature, and length are, respectively,

$$\begin{aligned} \rho_{\text{scale}} &= 1.67 \times 10^{-7} \text{ gm s}^{-1}, \\ v_{\text{scale}} &= c, \\ T_{\text{scale}} &= \mu m c^2 / k_B = 6.5 \times 10^{12} \text{ K}, \\ l_{\text{scale}} &= 1.48 \times 10^{13} \text{ cm}, \end{aligned}$$

where  $c$  is the speed of light, and the value of  $l_{\text{scale}}$  corresponds to the gravitational radius of a  $10^8 M_\odot$  black hole.

The gravitational potential due to a central point mass situated at the origin,  $\Phi$ , is modelled using a pseudo-Newtonian potential (Paczynski & Wiita 1980):

$$\Phi = \frac{-1}{r-2}. \quad (5)$$

Note that we take the gravitational radius (in scaled units),  $r_g = 1$ . The Schwarzschild radius,  $r_s = 2$  for a spherical black hole and the innermost stable circular orbit (ISCO) lies at  $r = 6$ .

A mass source term,  $\dot{M}_{\text{source}}$  is included in Eq (1) which relaxes the gas density within a narrow annulus spanning the outer  $\sim 12\%$  of the radial domain ( $31 \leq r \leq 34$ ,  $|z| < 2H$ ) towards the initial density distribution (see § 2.2) over a timescale of an orbital period, where  $H$  is the thermal disk scale-height. Including  $\dot{M}_{\text{source}}$  allows the total disk mass to reach a quasi-steady value, thus enabling long simulation runs. The  $\Lambda$  term on the RHS of Eq (3) is an ad-hoc cooling term used to keep the scale-height of the disk approximately constant throughout the simulations by driving the temperature distribution in the disk back towards the initial one over a timescale of an orbital period; without any explicit cooling in conjunction with an adiabatic equation of state, dissipation of magnetic and kinetic energy leads to an increase in gas pressure and, consequently, disk scale-height over time. The form of  $\Lambda$  is particularly simple (Parkin & Bicknell 2013a),

$$\Lambda = \frac{1}{(\gamma - 1)} \frac{T(R, z) - T_0(R)}{2\pi R / v_\phi} \quad (6)$$

where  $T_0(R)$  and  $T(R, z)$  are the position dependent initial and current temperature, respectively,  $v_\phi$  is the rotational velocity, and  $R$  is the cylindrical radius. Radiative cooling is applied using an operator-split approach at second-order accuracy.

The PLUTO code was configured to use the five-wave HLLD Riemann solver of Miyoshi & Kusano (2005), piecewise parabolic reconstruction (PPM - Colella & Woodward 1984), limiting during reconstruction on characteristic variables (e.g. Rider et al. 2007), second-order Runge-Kutta time-stepping, the upwind Constrained Transport scheme (Gardiner & Stone 2005a), and the FARGO-MHD module (which permits larger time steps in problems involving rapid rotation - see Mignone et al. 2012, for further details). For the FARGO-MHD module the background rotation profile was fixed to Keplerian rotation. To aid code stability, a small artificial viscous flux (with coefficient 0.1 - see Colella & Woodward 1984), which only switches on in regions of strong compression, is added to the Riemann solver fluxes. In addition to the above, to reduce the impact of high Alfvén speeds in the low density coronal region we have modified the PLUTO code to include the approximate Alfvén speed limiter suggested by Gombosi et al. (2002). This latter modification equates to replacing the conservative finite volume time update of Eq (2) with:

$$\left( \left( 1 + \frac{v_A^2}{c_{\text{lim}}^2} \right) \rho \mathbf{v} \right)_{n+1} = \left( \left( 1 + \frac{v_A^2}{c_{\text{lim}}^2} \right) \rho \mathbf{v} \right)_n + \Delta t \times \dots \quad (7)$$

where  $v_A$  is the Alfvén speed,  $c_{\text{lim}}$  is the reduced speed of light, and the subscript  $n$  denotes the time step number. The

above limiter has the advantage that steady-state solutions are independent of the choice of  $c_{\text{lim}}$ . Nevertheless, we choose the conservative value  $c_{\text{lim}} = 0.1$ , which is sufficient to aid with high values of  $v_A$  whilst being larger than the other wave speeds in the simulation.

The simulation grid uses  $(n_r, n_\theta, n_\phi) = (512, 256, 256)$  uniformly spaced cells, covering the spatial extent  $8 < r < 34$ ,  $\pi/2 - \theta_0 < \theta < \pi/2 + \theta_0$  (where  $\theta_0 = \tan^{-1}(3H/R)$ ), and  $0 < \phi < \pi/2$ . (The  $\theta$ -extent of the grid equates to  $|z| \pm 3H$  for a constant aspect ratio disk.) In terms of cells per scale height, the adopted grid has  $(n_r/H, n_\theta/H, n_\phi/H) \simeq (16-67, 43, 16)$  which is within the regime of convergence as a function of resolution found by Parkin & Bicknell (2013b). The adopted boundary conditions are identical to those used in Parkin & Bicknell (2013a) with the exception that for the  $\theta$ -boundaries we reflect density, pressure, and the normal velocity if the cell adjacent to the boundary is inflowing. This latter modification allows outflow whilst reducing spurious fluctuations in the cells adjacent to the  $\theta$ -boundary (Flock et al. 2011). A buffer zone, similar to that used by Fromang & Nelson (2006) and Flock et al. (2011) is used between  $8 \leq r \leq 12$  that has logarithmically increasing resistivity ( $\eta$ ) and viscosity ( $\nu$ ) with  $\eta_{\text{min}} = \nu_{\text{min}} = 10^{-6}$  and  $\eta_{\text{max}} = \nu_{\text{max}} = 10^{-4}$ . The resistive term is integrated explicitly, whereas super time stepping (see Mignone et al. 2007, and references therein) is used to integrate the viscous term. Finally, floor density and pressure values are used which scale linearly with radius and have values at the outer edge of the grid of  $10^{-3}$  and  $1.5 \times 10^{-6}$ , respectively.

With the combination of changes to the simulation algorithms described above (relative to that used in Parkin & Bicknell 2013a,b), an increase in average time step size by a factor of roughly 8-10 has been achieved. A sequence of simulations (not reported herein) was performed to assess the impact of the algorithmic modifications. The main difference introduced by the changes is an improved agreement between numerical dissipation and heating (which can be derived from the analysis in this work). In essence, this is an improvement in total energy conservation. The qualitative and quantitative results for turbulent stresses, magnetic energy, and kinetic energy are not affected by the changes to the algorithms.

## 2.2 Initial conditions

The simulation starts with an analytic equilibrium disk which is isothermal in height ( $T = T(R)$ , where  $T$  is the temperature) and possesses a purely toroidal net-flux magnetic field with a constant ratio of gas-to-magnetic pressure,  $\beta$ . The derivation of the disk equilibrium and a detailed description of the initial conditions can be found in Parkin & Bicknell (2013a). In cylindrical coordinates  $(R, z)$ , the density distribution, in scaled units, is given by,

$$\rho(R, z) = \rho(R, 0) \exp\left(\frac{-(\Phi(R, z) - \Phi(R, 0))}{T(R)} \frac{\beta}{1 + \beta}\right), \quad (8)$$

where the pressure,  $p = \rho T$ , and  $\beta = 2p/|B|^2 \equiv 2p/B_\phi^2$  is initially set to 20. The  $\theta$ -component of the vector potential,  $A_\theta$ , is used to initialise the magnetic field via  $\mathbf{B} = \nabla \times \mathbf{A}$  with,

$$A_\theta = \frac{1}{r} \int_{r_0}^r r B_\phi dr, \quad (9)$$

where  $r_0 = 7$  and  $A_\theta(r \leq r_0) = 0$ .

For the radial profiles  $\rho(R, 0)$  and  $T(R)$  in Eq (8) we use simple functions inspired by the Shakura & Sunyaev (1973) disk model, combined with an additional truncation of the density profile at a specified outer radius:

$$\rho(R, 0) = \rho_0 f(R, R_0, R_{\text{out}}) \left(\frac{R}{R_0}\right)^\epsilon, \quad (10)$$

$$T(R) = T_0 \left(\frac{R}{R_0}\right)^\eta, \quad (11)$$

where  $\rho_0$  sets the density scale,  $R_0$  and  $R_{\text{out}}$  are the radius of the inner and outer disk edge, respectively,  $f(R, R_0, R_{\text{out}})$  is a tapering function (Parkin & Bicknell 2013a), and  $\epsilon$  and  $\eta$  set the slope of the density and temperature profiles, respectively. Values are set to  $R_0 = 7$ ,  $R_{\text{out}} = 50$ ,  $\rho_0 = 10$ ,  $\epsilon = -33/20$ ,  $\eta = -9/10$ , and  $T_0 = 1.5 \times 10^{-3}$ , producing a disk with  $H/R = 0.1$ . Note that in contrast to the simulations in Parkin & Bicknell (2013a,b), which focused on a finite disk mass residing within a larger simulation domain, the adopted grid position and extent in this work places the simulation domain *within* the disk (e.g. Fromang & Nelson 2006; Flock et al. 2011).

The rotational velocity of the disk is close to Keplerian, with a minor modification due to the gas and magnetic pressure gradients,

$$v_\phi^2(R, z) = v_\phi^2(R, 0) + (\Phi(R, z) - \Phi(R, 0)) \frac{R}{T} \frac{dT}{dR}, \quad (12)$$

where,

$$v_\phi^2(R, 0) = R \frac{\partial \Phi(R, 0)}{\partial R} + \frac{2T}{\beta} + \left(\frac{1 + \beta}{\beta}\right) \left(\frac{RT}{\rho(R, 0)} \frac{\partial \rho(R, 0)}{\partial R} + R \frac{dT}{dR}\right). \quad (13)$$

To initiate the development of turbulence in the disk, we add random poloidal velocity fluctuations of amplitude  $0.01 c_s$ , where  $c_s$  is the sound speed, to the initial equilibrium.

## 2.3 Diagnostic averages

A volume-averaged value (denoted by angled brackets) for a variable  $q$  is computed via,

$$\langle q \rangle = \frac{\iiint q r^2 \sin \theta dr d\theta d\phi}{\iiint r^2 \sin \theta dr d\theta d\phi}. \quad (14)$$

Similarly, azimuthal averages are denoted by square brackets,

$$[q] = \frac{\int q r \sin \theta d\phi}{\int r \sin \theta d\phi}. \quad (15)$$

The analysis in the remainder of this paper concentrates on the ‘‘disk body’’ which is defined as the region between  $15 < r < 25$  and  $|z| < 2H$ . We also make use of time averages, all of which are computed over the interval  $20 < t < 40 P_{30}^{\text{orb}}$ , where  $P_{30}^{\text{orb}}$  corresponds to the orbital period at a radius,  $r = 30$ . This time interval corresponds to the latter half of the simulation, when a quasi-steady state has been reached (see § 3).

**Table 1.** Time averaged simulation diagnostics. Values are spatially averaged within the disk body (§ 2.3) and time averaged over the interval  $20 \leq t \leq 40 P_{30}^{\text{orb}}$ . See § 3 for symbol definitions.

Parameter	Value	Parameter	Value
$N_r$	0.76	$\langle \beta_r \rangle$	118
$N_\theta$	0.65	$\langle \beta_\theta \rangle$	316
$N_\phi$	0.81	$\langle \beta_\phi \rangle$	20
$\langle \alpha_P \rangle$	0.036	$\langle \beta_{\text{tot}} \rangle$	16
$\langle \alpha_M \rangle$	0.47	$-\langle B'_r B'_\phi \rangle / \langle \rho v'_r v'_\phi \rangle$	2.69

## 2.4 Mean and turbulent fields

In our analysis we decompose the velocity and magnetic fields into mean and turbulent components. For this purpose we define the mean field to be the azimuthal average of the velocity/magnetic field at a given  $r$  and  $\theta$ . The turbulent velocity and magnetic fields are then given by,

$$v_i = v'_i + \bar{v}_i, \quad \text{where,} \quad \bar{v}_i = [\rho v_i] / [\rho] \quad (16)$$

and,

$$B_i = B'_i + \bar{B}_i, \quad \text{where,} \quad \bar{B}_i = [B_i] \quad (17)$$

where over-bars and primes indicate mean and turbulent components, respectively. The corresponding mean and turbulent magnetic energies are defined as  $u_{\bar{B}} = \frac{1}{2} |\bar{B}|^2$  and  $u_{B'} = \frac{1}{2} |B'|^2$ , respectively, and the turbulent kinetic energy is given by,  $u_{K'} = \frac{1}{2} \rho |v'|^2$ . Note that a mass-weighted average is used for velocities as it simplifies terms in the mean-field equations, particularly the turbulent kinetic energy, and also ensures that the mean flow conserves mass (Favre 1969; Kuncic & Bicknell 2004). Furthermore, for a mass-weighted average, the averaged total kinetic energy is the sum of the mean and turbulent kinetic energies,  $[\rho v^2] = [\rho \bar{v}^2] + [\rho v'^2]$ . In § 4 we perform statistical (Reynolds) averaging for various equations, following the standard rules for averaging (see, e.g., Davidson 2004; Kuncic & Bicknell 2004). For example,  $[B'_i] = \bar{B}'_i = 0$ ,  $[B'_i B'_j \bar{v}_{i;j}] = \bar{B}'_i \bar{B}'_j \bar{v}_{i;j}$ , and  $[B'_i \bar{B}_j \bar{v}_{i;j}] = 0$ . In addition, azimuthally-averaged equations will be converted to volume-averaged ones using an intermediate meridional-average (i.e. over the  $r, \theta$  plane):

$$\frac{\iint [f] r dr d\theta}{\iint r dr d\theta} \equiv \frac{\iiint f r^2 \sin \theta dr d\theta d\phi}{\iiint r^2 \sin \theta dr d\theta d\phi} = \langle f \rangle. \quad (18)$$

Note that this latter operation commutes because azimuthal averages are computed at a specific  $r$  and  $\theta$ . Hence,  $\int r \sin \theta d\phi \iint r dr d\theta \equiv \iiint r^2 \sin \theta dr d\theta d\phi$ .

## 3 CHARACTERISING THE DISK TURBULENCE

### 3.1 Turbulent stresses

To quantify the efficiency of angular momentum transport due to the  $r - \phi$  component of the combined Reynolds and Maxwell stress, we compute the Shakura & Sunyaev (1973)  $\alpha$ -parameter (Table 1),

$$\langle \alpha_P \rangle = \frac{\langle \rho v'_r v'_\phi - B'_r B'_\phi \rangle}{\langle p \rangle}, \quad (19)$$

where we have defined the turbulent components, denoted by primes, as described in § 2.4. This approach has been

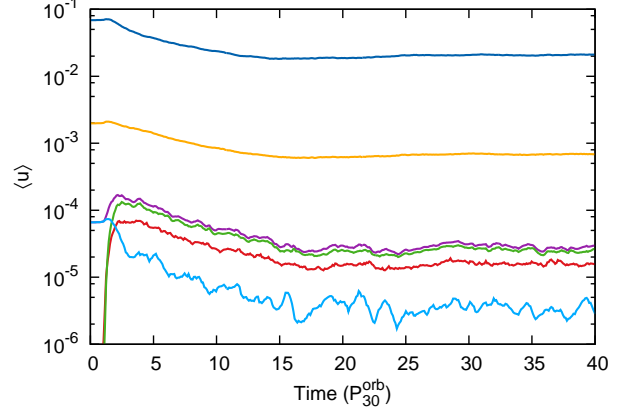


**Figure 1.** The time evolution of volume averaged values for various energies (computed over the disk body): total kinetic (dark blue), internal (orange), total magnetic (purple), turbulent magnetic (green), turbulent kinetic (red), and mean magnetic (light blue). Time is in units of the orbital period at a radius of  $r = 30$ ,  $P_{30}^{\text{orb}}$ . (For comparison,  $P_{30}^{\text{orb}} = 9 P_8^{\text{orb}}$ , therefore roughly 360 inner disk orbits are covered.) The mean kinetic energy is not plotted as it is indistinguishable from the total kinetic energy on this plot. Time averaged values for energies are noted in Table 2.

shown above, and by Flock et al. (2011), to remove the influence of strong vertical and radial gradients when computing averaged values. In addition, we calculate the  $r - \phi$  component of the Maxwell stress normalised by the magnetic pressure,

$$\langle \alpha_M \rangle = \frac{\langle -2B'_r B'_\phi \rangle}{\langle |B'|^2 \rangle}. \quad (20)$$

The value of  $\langle \alpha_P \rangle = 0.036$  is in agreement with the models within the regime of convergence reported by Parkin & Bicknell (2013b), and  $\langle \alpha_M \rangle = 0.47$  agrees with the well-resolved models presented by Parkin & Bicknell (2013a,b) and Hawley et al. (2013) - additional tests have confirmed that the slightly higher value of  $\langle \alpha_M \rangle$  compared to previous work results from using the turbulent, rather than total, magnetic fields in Eq (20). Furthermore, the ratio of Maxwell-to-Reynolds stress,  $-\langle B'_r B'_\phi \rangle / \langle \rho v'_r v'_\phi \rangle = 2.69$  is consistent with previous global disk studies (Fromang & Nelson 2006; Beckwith et al. 2011).

### 3.2 MRI-resolution

To demonstrate that the simulation is sufficiently well resolved we quote time-averaged values for the resolvability,  $N_i$ , which is defined to be the fraction of cells in the disk body that resolve the wavelength of the fastest growing MRI mode,  $\lambda_{\text{MRI-i}}$ , with at least 8 cells<sup>1</sup>, where,

$$\lambda_{\text{MRI-i}} = \frac{2\pi |v_{\text{Ai}}| r \sin \theta}{v_\phi}, \quad (21)$$

<sup>1</sup> This equates to measuring the fraction of cells which have a “quality factor” (Noble et al. 2010; Hawley et al. 2011) which is 8 or better throughout the disk - see also Sorathia et al. (2012) and Parkin & Bicknell (2013b).



**Table 2.** Time averaged energies. Values are spatially averaged within the disk body (§ 2.3) and time averaged over the interval  $20 \leq t \leq 40 P_{30}^{\text{orb}}$ . See § 3 for symbol definitions. See Fig. 1 for the corresponding time evolution of these energies.

$\langle u_K \rangle$ ( $10^{-2}$ )	$\langle u_{K'} \rangle$ ( $10^{-5}$ )	$\langle u_B \rangle$ ( $10^{-5}$ )	$\langle u_{B'} \rangle$ ( $10^{-5}$ )	$\langle u_{\bar{B}} \rangle$ ( $10^{-6}$ )	$\langle u_\varepsilon \rangle$ ( $10^{-4}$ )
2.0	1.6	2.8	2.5	3.5	6.7

where  $i = r, \theta, \phi$ , and  $v_{\text{Ai}} = B_i / \sqrt{\rho}$  is the Alfvén speed. The simulation achieves time-averaged values for the resolvability of  $N_r = 0.76$ ,  $N_\theta = 0.65$ , and  $N_\phi = 0.81$ , indicating an adequate resolution of MRI modes (Sorathia et al. 2012; Parkin & Bicknell 2013b). Further discussion of the resolution of the MRI in similar stratified global models can be found in Fromang & Nelson (2006), Flock et al. (2011), Hawley et al. (2011, 2013), Parkin & Bicknell (2013a,b), and Suzuki & Inutsuka (2013).

### 3.3 Mean and turbulent fields/energies

The time evolution of the various disk-body-volume-averaged energies is shown in Fig. 1, with the corresponding time-averaged values noted in Table 2. The total energy content of the disk is dominated by the total kinetic energy, which is mainly due to the mean disk rotation. The internal energy is the next largest energy, followed by the total magnetic energy. Decomposing the kinetic and magnetic energies into mean and turbulent components (see § 2.4), one sees that the turbulent kinetic and magnetic energies are subthermal (i.e. less than the internal energy). Furthermore, the turbulent kinetic energy makes up a meagre 0.1% of the total kinetic energy, whereas more than 90% of the magnetic energy resides in the turbulent field, with the remaining  $\sim 10\%$  in the mean magnetic field.

Examining the vertical and radial profiles for mean magnetic fields in more detail (Fig. 2), one sees relatively little variation of  $\bar{B}_\theta$  as a function of height below  $|z| < 2H$ . There is an apparent anti-correlation between  $\bar{B}_r$  and  $\bar{B}_\phi$ , arising from the negative shear found in Keplerian rotation. The mean azimuthal magnetic field, on average, increases with decreasing radius. The mean velocity field is dominated by (almost) Keplerian rotation, where,

$$v_{\text{Kep}} = \left( r \frac{d\Phi}{dr} \right)^{1/2} = \frac{r^{1/2}}{r-2}, \quad (22)$$

with  $1 - \bar{v}_\phi / v_{\text{Kep}} \simeq 0.01$  at  $r = 20$ . However, Fig. 2 shows that at larger heights in the coronal region ( $|z| > 2H$ ) the mean rotation is increasingly sub-Keplerian. In the radial direction, the mean rotation transitions from sub- to supra-Keplerian at  $r \simeq 13$ . The mean radial flow,  $\bar{v}_r$ , is of larger magnitude than the vertical flow<sup>2</sup>,  $\bar{v}_\theta$ , and is predominantly inflowing onto the central object. Examining the variation of  $\bar{v}_r$  with height shows that inflow velocities peak above and below the mid plane at a height in the region of  $H \leq |z| \leq 2H$ . Furthermore, at  $r > 28$  (which is outside of the radial extent we consider for our “disk body” analysis) the mean radial flow is *outflowing* which is most likely the

consequence of some mass carrying away angular momentum (hence allowing accretion). There is a weak vertical outflow at the upper/lower domain boundaries, although we are apprehensive about designating it to be a “wind” as its associated mass-loss rate is negligible compared to that arising from radial inflow within the disk body. Furthermore, the vertical flows are substantially below the escape velocity.

Turning next to the turbulent fields, the simulation snapshots of the velocity and magnetic fields shown in Figs 3 and 4, respectively, indicate that the radial and azimuthal fluctuations are the largest. In terms of the characteristic shape and magnitude of the fluctuations, the turbulent velocity and magnetic fields look notably different. However, they have common features in the elongation of structures in the direction of rotation and the inhomogeneous distribution of fluctuations.

Constructing vertical and radial profiles of the amplitude (i.e. absolute value) of the turbulent components (Fig. 5), shows that both magnetic and velocity fields exhibit little variation in the region close to the mid plane  $|z| < H$ , with radial velocity perturbations and azimuthal magnetic field perturbations having the largest amplitudes. In the coronal region ( $|z| > 2H$ ) there is anti-correlated behaviour between magnetic and velocity field amplitudes; the amplitude of the turbulent magnetic field falls off with height, whereas turbulent velocities grow in amplitude with height. The turn-down in  $|v'_\theta|$  close to the vertical boundaries is likely due to reflected waves inhibiting outflow<sup>3</sup>. The rise in the amplitude of the turbulent fields going from larger to smaller radii is the anticipated effect of a rising Keplerian velocity at smaller radii, and thus a larger reservoir of kinetic energy from which the MRI can drive the turbulence. There is a rise in  $|v'_r|$  and  $|v'_\theta|$  at  $r > 25$  which may be associated with the outflow seen in the mean radial velocity and the decrease in the mean disk rotation at these radii (Fig. 2). The run of turbulent velocity amplitudes observed in Fig. 5 is consistent with those found in similar models by Fromang & Nelson (2006), Flock et al. (2011), and Beckwith et al. (2011). Turbulent magnetic field amplitudes bear the same ordering in height and radius as found by Flock et al. (2011), however we do not find a dip in the vertical profile at the mid plane for  $|B'_r|$  and  $|B'_\theta|$ , rather we observe gently peaked profiles.

The results simulation results provide valuable information for models of coronal powering based on the buoyant advection of turbulent structures (e.g. Blackman & Pessah 2009; Uzdensky 2013). For instance, the prominence of mean radial flow over mean vertical flow rules out advection by the latter for powering coronae. However, close to the mid plane of the disk ( $|z| < 2H$ ), the turbulent vertical motions are of greater magnitude than the mean radial flow. As such, coronal powering could be realized by buoyant rising associated with turbulent motions, provided a sufficient correlation between regions of strong magnetic field and such motions exists.

In Fig. 6 we show power spectra for the radial, vertical ( $\theta$ -direction), and azimuthal field components of the tur-

<sup>2</sup> Note that, as plotted in Fig. 2, a positive  $\bar{v}_\theta$  points away from the mid plane when  $z/H$  is positive, and vice-versa.

<sup>3</sup> Suzuki & Inutsuka (2009) suggest that reflected waves can be avoided by explicitly treating outgoing waves at boundaries using a characteristic decomposition.

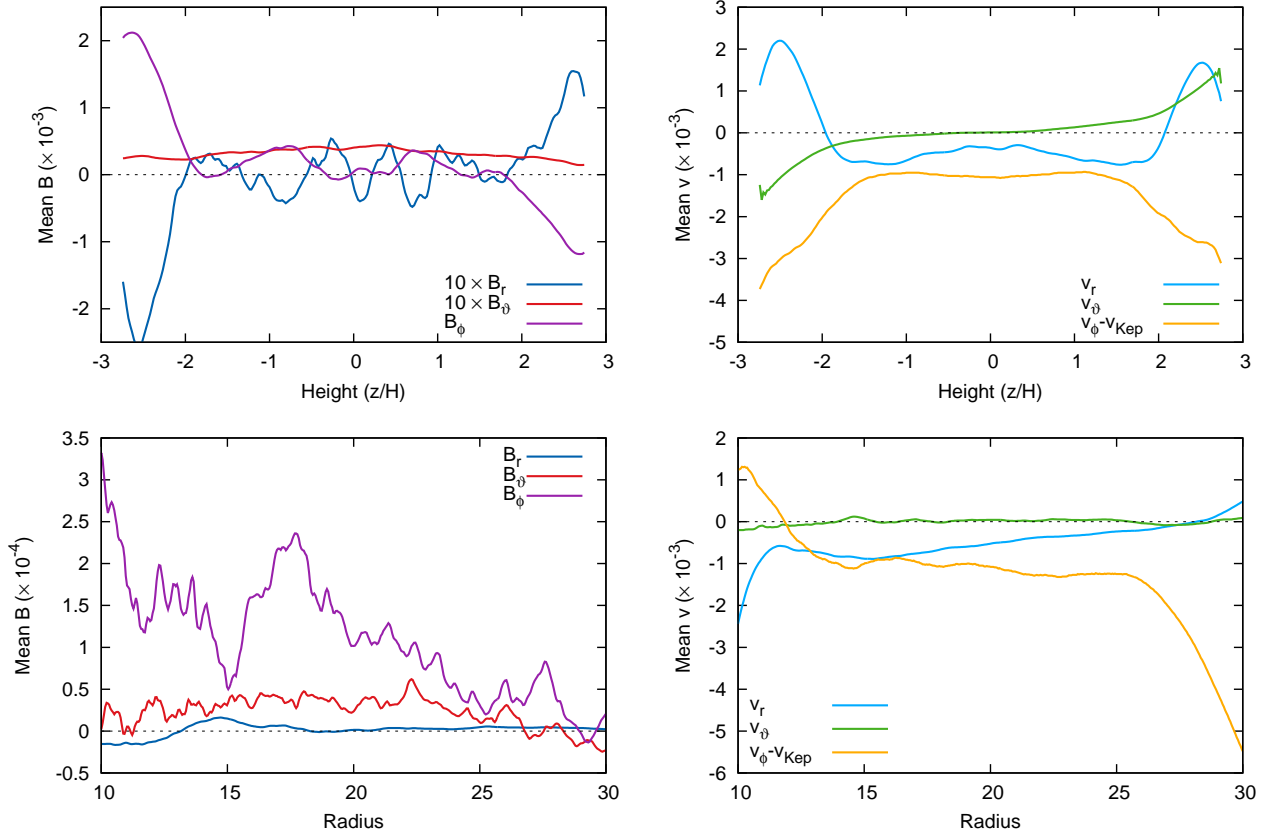


**Figure 2.** Time averaged profiles for mean magnetic (left column) and velocity (right column) fields. The top row shows vertical profiles, which were computed by radially averaging the azimuthal mean at a given  $\theta$  between  $15 < r < 25$ . The lower row shows radial profiles, which were computed by vertically averaging (within  $|z| < 2H$ ) the azimuthal mean at a given radius. Time averages were computed over the interval  $20 < t < 40 P_{30}^{\text{orb}}$ . In the upper left plot values of  $\bar{B}_r$  and  $\bar{B}_\theta$  have been multiplied by a factor of 10 to aid comparison.

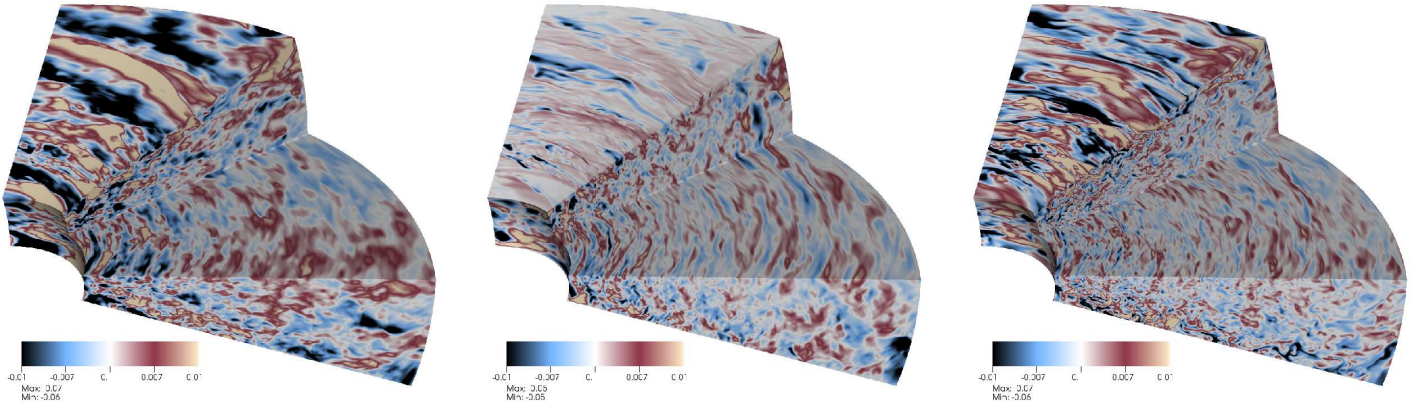


**Figure 3.** Snapshots of the turbulent velocity fields at  $t = 30 P_{30}^{\text{orb}}$ . From left to right:  $v'_r$ ,  $v'_\theta$ , and  $v'_\phi$ . The images show a 3D view of the simulation domain with a section of the upper hemisphere removed, exposing the mid plane.

turbulent magnetic and velocity fields. We define the Fourier transform of a function  $q(r, \theta, \phi)$  as,

$$Q(\mathbf{k}) = Q(k, \chi, \psi) = \int_0^{2\pi} \int_0^\pi \int_0^\infty q(r, \theta, \phi) e^{i\mathbf{k} \cdot \mathbf{x}} \times r^2 \sin \theta dr d\theta d\phi, \quad (23)$$

where  $k$  is the radial wavenumber and  $(\chi, \psi)$  are angular coordinates in Fourier space. It then follows that the angle-averaged (in Fourier space) amplitude spectrum,

$$|Q(k)|^2 = \int_0^{2\pi} \int_0^\pi Q(\mathbf{k}) Q^*(\mathbf{k}) \sin \chi d\chi d\psi, \quad (24)$$

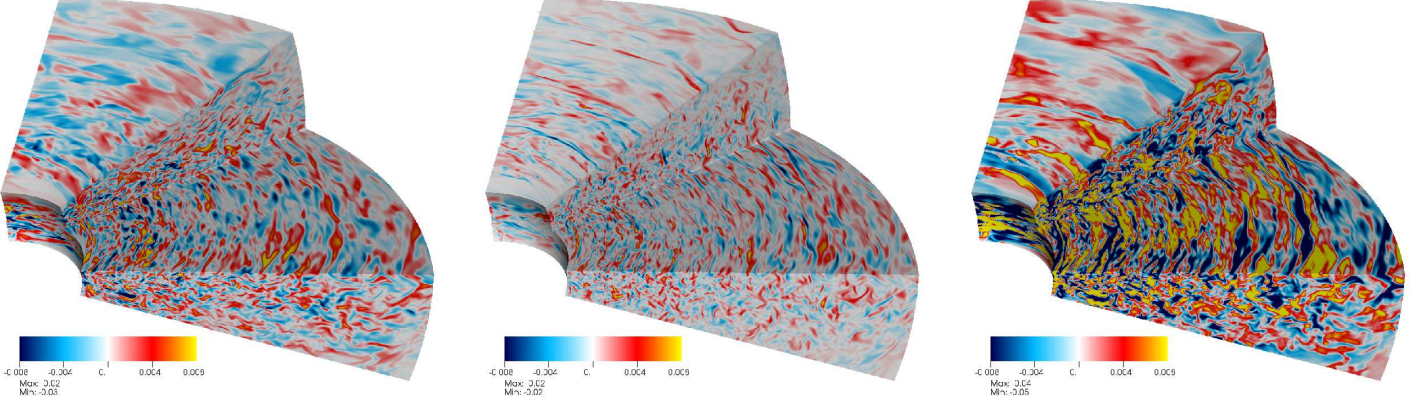


**Figure 4.** Same as Fig. 3 except for the turbulent magnetic field:  $B'_r$  (left),  $B'_\theta$  (middle), and  $B'_\phi$  (right).

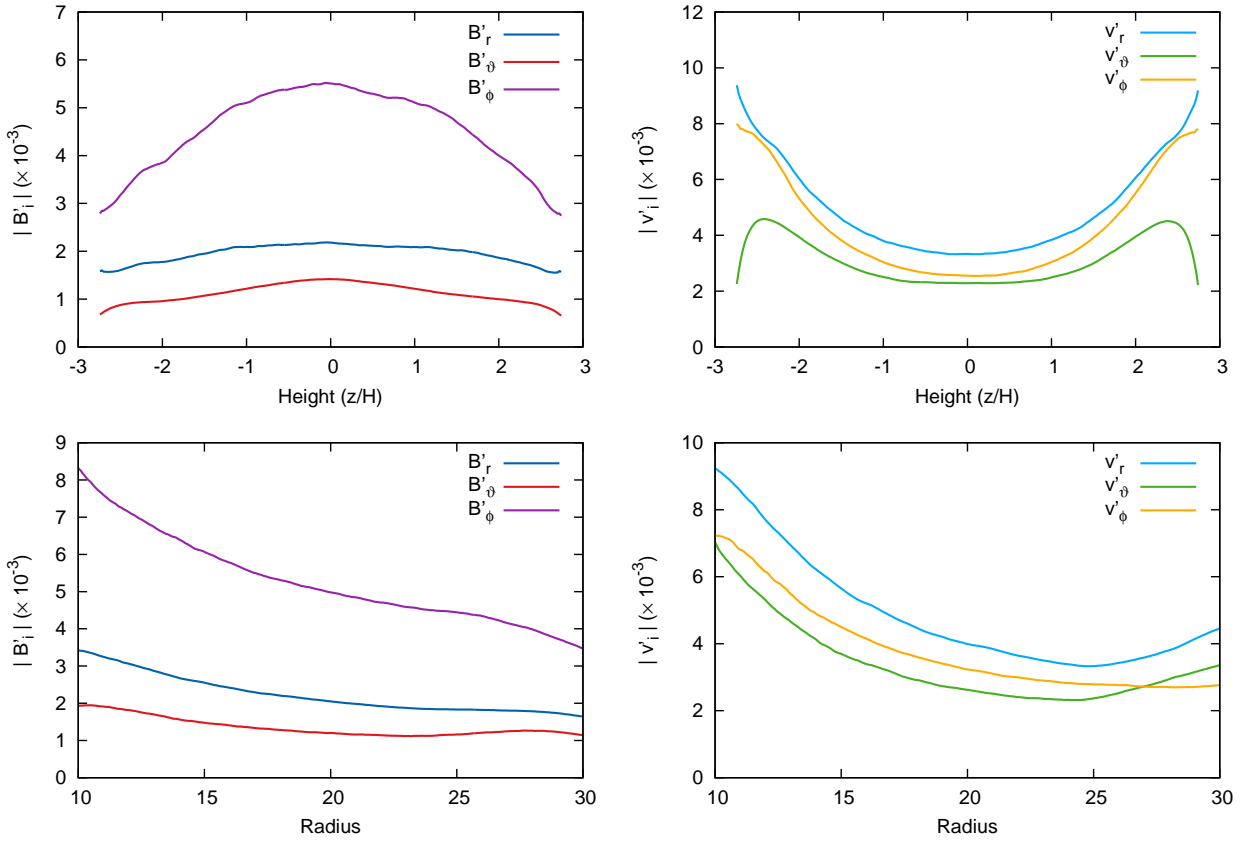


**Figure 5.** Time averaged profiles for the magnitude of turbulent magnetic (left column) and velocity (right column) fields. The top row shows vertical profiles, which were computed by radially and azimuthally averaging the turbulent field at a given  $\theta$  and between  $15 < r < 25$  in radius and the full domain extent ( $0 < \phi < \pi/2$ ) in the azimuthal direction. The lower row shows radial profiles, which were computed by vertically and azimuthally averaging the turbulent field the azimuthal mean at a given radius and within  $|z| < 2H$ . Time averages were computed over the interval  $20 < t < 40 P_{30}^{\text{orb}}$ .

where an asterisk (\*) indicates a complex conjugate. The total power at a given wavenumber - the power spectrum - is given by  $k^2|Q(k)|^2$ . For each spectrum shown in Fig. 6, an average was taken over 200 individual spectra computed for the disk body region (see § 2.3) from simulation data files equally spaced in time in the interval  $20 < t < 40 P_{30}^{\text{orb}}$ . The

Fourier transforms were computed in spherical coordinates using the method outlined in Parkin & Bicknell (2013b).

The power spectra provide information about the orientation of the fluctuating magnetic/velocity fields on different spatial scales. As such, they allow a quantification of properties of the turbulence suggested from a visual inspection of

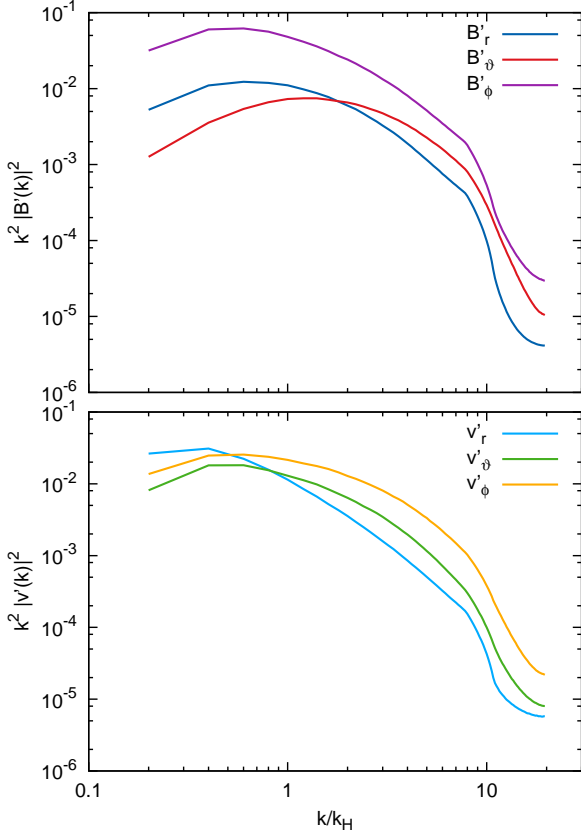


**Figure 6.** Angle-averaged power spectra for the turbulent magnetic (upper) and velocity (lower) fields, showing the separate directional contributions. The horizontal axis is in units of  $k/k_H = 2\pi/\langle H \rangle$ .

Figs. 3 and 4. Examining the upper panel of Fig. 6, one sees that azimuthal magnetic field dominates at all scales. However, the ordering of the radial and vertical magnetic field components differs between the largest ( $k < k_H$ ) and smallest scales ( $k > k_H$ ); on the largest scales  $|B'_r(k)|^2 > |B'_\theta(k)|^2$ , and vice-versa on the smallest scales. The same is true for the power spectra of the turbulent velocity components. In fact, on the very largest scales ( $k/k_H < 0.4$ ), radial velocity fluctuations are more powerful than those for the azimuthal components, whereas close to the dissipation scale  $|v'_r(k)|^2$  is smaller than both  $|v'_\theta(k)|^2$  and  $|v'_\phi(k)|^2$ . The above results indicate an important deviation from Kolmogorov-type turbulence in that anisotropy is not removed as energy cascades to smaller scales. To the contrary, accretion disk turbulence is anisotropic at all scales. However, the order of strengths for different directional contributions changes, with a possible implication that the underlying turbulent dynamo may change character at different length scales (see also the discussion by Davis et al. 2010).

In summary, the simulations resolve the MRI sufficiently well to achieve a quasi-steady turbulent state in which  $\langle \alpha_P \rangle$  is approximately constant from  $t \gtrsim 15 P_{30}^{\text{orb}}$  onwards. The addition of a mass source term to the simulation setup (see § 2) allows the total disk mass to stabilise, and this in turn produces quasi-steady energies in the post-transient phase ( $t \gtrsim 20 P_{30}^{\text{orb}}$  - Fig. 1). The mean velocity

field is dominated by (essentially) Keplerian rotation. There are no obvious underlying gradients in the averaged turbulent velocity and magnetic fields, indicating that the adopted decomposition of mean and turbulent fields is effective.

## 4 CONTROL VOLUME ANALYSIS

In the previous section we provided a general qualitative view of a turbulent accretion disk. The purpose of this section is to assess the roles of the mean and turbulent fields in driving the energy budget of the disk. This involves evaluating mean-field, Reynolds averaged equations using the simulation data, and to this end we examine the mean and turbulent magnetic energies, mean field induction equation, turbulent kinetic energy, and the internal energy. The equations are general. However, the analysis focuses on the disk body region (defined in § 2.3) the boundaries of which are open in the radial and vertical directions, and periodic in the azimuthal direction.

### 4.1 Turbulent magnetic energy evolution

The derivation of the turbulent magnetic energy equation begins with the magnetic field induction equation, to which we add a term for *numerical* resistive losses,  $d_i^{\text{res}}$ , such that Eq (4) now reads,

$$\frac{\partial B_i}{\partial t} = \nabla \times (\mathbf{v} \times \mathbf{B}) + d_i^{\text{res}}. \quad (25)$$

The  $d_i^{\text{res}}$  term encapsulates the dissipation due to the truncated order of accuracy of numerical finite volume codes (such as the PLUTO code used in this investigation). In essence,  $d_i^{\text{res}}$  is a place-holder for an adopted/relevant form for the resistive term. Next we expand the magnetic and velocity fields in Eq (25) into mean and turbulent components (see § 2.4), take the scalar product of  $B'_i$  with the resulting equation, and then azimuthally (Reynolds) average. After a little algebra, one has,

$$\begin{aligned} \frac{\partial \overline{u_{B'}}}{\partial t} &= -\overline{\mathcal{P}'_{k,k}} + \overline{B_j B'_i v'_{i,j}} + \overline{B'_i B'_j \bar{v}_{i,j}} - 2 \frac{\partial}{\partial x_j} (\overline{u_{B'} \bar{v}_j}) \\ &\quad - \overline{B'_i v'_j \bar{B}_{i,j}} - \overline{B_i B'_j v'_{k,k}} - v'_i \frac{\partial M'_{ij}}{\partial x_j} + \overline{B'_i d_i^{\text{res}}}, \end{aligned} \quad (26)$$

where a subscript comma denotes partial differentiation, a subscript semicolon denotes a covariant derivative, and we recall that an over-bar indicates an azimuthal average and that  $u_{B'}$  is the turbulent magnetic energy. The Poynting vector,

$$\mathcal{P}_j = |B|^2 v_j - v_i B_i B_j = u_B v_j - v_i M_{ij}, \quad (27)$$

and the Maxwell stress tensor,

$$M_{ij} = B_i B_j - \delta_{ij} u_B. \quad (28)$$

Note, for example, that  $\mathcal{P}'_j$  indicates the turbulent Poynting vector, whereby all composite velocity and magnetic fields are turbulent also, with the same being true for the turbulent Maxwell stress tensor,  $M'_{ij}$ . The final step is to take an average of Eq (26) over a meridional ( $r, \theta$ ) plane, thus converting azimuthal averages into an average over a volume,



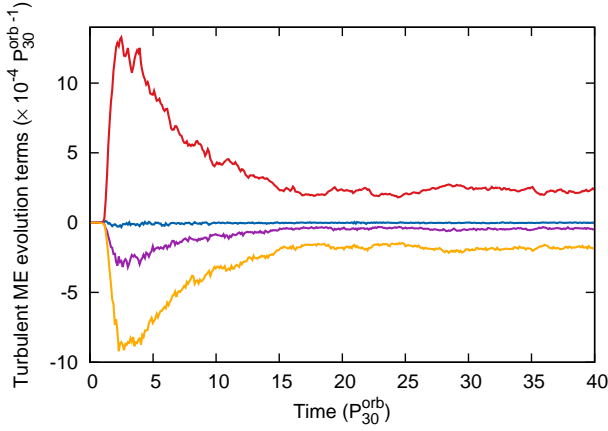


**Figure 7.** Turbulent magnetic energy evolution (see § 4.1). Shown are:  $\langle F_{\mathcal{P}'} \rangle$  (blue),  $\langle \mathcal{S}_{B'} \rangle$  (red),  $\langle \mathcal{L}' \rangle$  (purple), and  $\langle D_{B'}^{\text{res}} \rangle$  (orange). Positive values indicate energy input, whereas negative values indicate removal of energy.

$V$ , with bounding surface,  $s$  - see § 2.4 and Eq (18). The volume averaged turbulent magnetic energy equation reads,

$$\begin{aligned} \langle \dot{u}_{B'} \rangle &= \langle B'_i \bar{B}_j v'_{i,j} \rangle - \langle B'_i v'_j \bar{B}_{i,j} \rangle - \langle B'_i \bar{B}_i v'_{k,k} \rangle + \left\langle \bar{v}_j \frac{\partial u_{B'}}{\partial x_j} \right\rangle \\ &\quad \langle F_{\mathcal{P}'} \rangle + \langle \mathcal{S}_{B'} \rangle + \langle \mathcal{L}' \rangle + \langle F_{u_{B'}} \rangle + \langle D_{B'}^{\text{res}} \rangle, \end{aligned} \quad (29)$$

where we have introduced the additional symbols:

$$\langle \dot{u}_{B'} \rangle = \frac{\partial}{\partial t} \langle u_{B'} \rangle, \quad (30)$$

$$\langle F_{\mathcal{P}'} \rangle = -\langle \mathcal{P}'_{k,k} \rangle = -\frac{1}{V} \int_s \mathcal{P}'_k ds_k, \quad (31)$$

$$\langle F_{u_{B'}} \rangle = -2 \left\langle \frac{\partial}{\partial x_k} (u_{B'} \bar{v}_k) \right\rangle = -\frac{2}{V} \int_s u_{B'} \bar{v}_k ds_k, \quad (32)$$

$$\langle \mathcal{S}_{B'} \rangle = \langle B'_i B'_j \bar{v}_{i,j} \rangle \quad (33)$$

$$\langle \mathcal{L}' \rangle = - \left\langle v'_i \frac{\partial M'_{ij}}{\partial x_j} \right\rangle, \quad (34)$$

$$\langle D_{B'}^{\text{res}} \rangle = \langle B'_i d_i^{\text{res}} \rangle. \quad (35)$$

The symbols in equations (30)-(35) have the following meanings: the volume averaged rate of change of magnetic energy is given by  $\langle \dot{u}_{B'} \rangle$ ,  $\langle \mathcal{S}_{B'} \rangle$  represents energy production by a stress-shear correlation between turbulent Maxwell stresses and mean flow shear,  $\langle F_{\mathcal{P}'} \rangle$  is the turbulent Poynting flux,  $\langle F_{u_{B'}} \rangle$  is the advective flux of turbulent magnetic energy in/out of the disk via the mean flow, and energy extraction due to turbulent Lorentz forces doing work on the disk is given by  $\langle \mathcal{L}' \rangle$ . Finally,  $\langle D_{B'}^{\text{res}} \rangle$  denotes resistive dissipation. Note that all terms featuring in Eqs (29)-(35) can be explicitly evaluated using the simulation data. This is one benefit of this approach as one can evaluate the (numerical) dissipation,  $D_{B'}^{\text{res}}$ , without knowledge of the functional form of the dissipation term. Note that, in this regard, the control volume approach bears similarities with Fourier analysis methods adopted by Fromang & Papaloizou (2007) and Simon et al. (2009). Moreover, Parseval's theorem equates total power in real space and Fourier space, hence the total power in correlated terms will be the same whether one evaluates them in real space or Fourier space.

Fig. 7 shows results for the largest terms in the turbulent magnetic energy equation (Eq 29) - time-averaged values for all terms are noted in Table 3. One sees that the combination of Maxwell stresses and shear in the mean velocity field ( $\langle \mathcal{S}_{B'} \rangle$ ) is responsible for injecting most of the magnetic power, which is then removed via (in this case numerical) resistive dissipation ( $\langle D_{B'}^{\text{res}} \rangle$ ). This is a very similar conclusion to that found by Parkin & Bicknell (2013b), who performed a similar analysis of the total magnetic energy equation; the present study makes the advance of rigorously separating mean and turbulent fields.

The rate of change of turbulent magnetic energy ( $\langle \dot{u}_{B'} \rangle$ ) has a net positive value, although the variance is larger than the mean (Table 3). The turbulent Poynting flux ( $\langle F_{\mathcal{P}'} \rangle$ ) has little impact on the energy balance, similarly advection of turbulent magnetic energy in/out of the disk by the mean flow ( $\langle \bar{v}_j \frac{\partial u_{B'}}{\partial x_j} \rangle$ ) is relatively small (Table 3). The second largest contribution to energy removal is due to turbulent Lorentz forces ( $\langle \mathcal{L}' \rangle$ ). We show in § 4.5 that this term is responsible for converting turbulent magnetic energy into turbulent kinetic energy.

It is noteworthy that the largest contribution to the turbulent magnetic energy is not associated with the mean magnetic field, but with the turbulent Maxwell stress and the mean velocity field (essentially time-steady Keplerian rotation). This would suggest that, despite exhibiting periodic oscillatory behaviour indicative of dynamo variability (§ 4.3 - see also Fromang & Nelson 2006; Gressel 2010; O'Neill et al. 2011; Oishi & Mac Low 2011; Flock et al. 2012a; Parkin & Bicknell 2013b), mean magnetic fields do not play a significant direct part in replenishing the turbulent magnetic energy. Hence, the role of the mean magnetic field is not immediately evident from an analysis of the turbulent magnetic energy alone. We return to this point in §§ 4.2 and 4.3.

## 4.2 Mean magnetic energy evolution

The derivation of the mean magnetic energy equation proceeds in a similar manner as that for the turbulent magnetic energy equation in the previous section. The main difference is that, after expanding fields into mean and turbulent components in Eq (25), one takes the scalar product with  $\bar{B}_i$  before Reynolds averaging in the azimuthal direction, followed by a meridional ( $r, \theta$ ) averaging. The result is:

$$\begin{aligned} \langle \dot{u}_{\bar{B}} \rangle &= \langle \mathcal{S}_{\bar{B}} \rangle + \langle \bar{B}_i B'_j v'_{i,j} \rangle - \langle \bar{B}_i v'_j B'_{i,j} \rangle \\ &\quad - \langle \bar{B}_i B'_i v'_{k,k} \rangle + \langle F_{u_{\bar{B}}} \rangle + \left\langle \bar{v}_i \frac{\partial u_{\bar{B}}}{\partial x_i} \right\rangle + \langle D_{\bar{B}}^{\text{res}} \rangle, \end{aligned} \quad (36)$$

where we have introduced the following symbols:

$$\langle \dot{u}_{\bar{B}} \rangle = \frac{\partial}{\partial t} \langle u_{\bar{B}} \rangle, \quad (37)$$

$$\langle \mathcal{S}_{\bar{B}} \rangle = \langle \bar{B}_i \bar{B}_j \bar{v}_{i,j} \rangle \quad (38)$$

$$\langle F_{u_{\bar{B}}} \rangle = -2 \left\langle \frac{\partial}{\partial x_k} (u_{\bar{B}} \bar{v}_k) \right\rangle = -\frac{2}{V} \int_s u_{\bar{B}} \bar{v}_k ds_k, \quad (39)$$

$$\langle D_{\bar{B}}^{\text{res}} \rangle = \langle \bar{B}_i d_i^{\text{res}} \rangle, \quad (40)$$

and where  $u_{\bar{B}} = \frac{1}{2} |\bar{B}|^2$ . The results of evaluating Eq (36) using the simulation data are shown Fig. 8, with time-averaged values for all terms noted in Table 3. The mean magnetic field energy is self-generated in the sense that the dominant

**Table 3.** Time averaged values for terms pertaining to the control volume analysis. Terms are grouped (from left to right, top to bottom): turbulent magnetic energy, mean magnetic energy, total Poynting flux, turbulent Poynting flux, turbulent kinetic energy, and internal energy. Time averages are computed over the interval  $20 < t < 40 P_{30}^{\text{orb}}$ .

Term	Value ( $\times 10^{-6} P_{30}^{\text{orb}-1}$ )	Term	Value ( $\times 10^{-6} P_{30}^{\text{orb}-1}$ )
Turbulent magnetic energy		Mean magnetic energy	
$\langle \dot{u}_{B'} \rangle$	$0.043 \pm 0.36$	$\langle \dot{u}_{\bar{B}} \rangle$	$-0.066 \pm 0.19$
$\langle F_{\mathcal{P}'} \rangle$	-1.1	$\langle \mathcal{S}_{\bar{B}} \rangle$	14.6
$\langle F_{u_{B'}} \rangle$	-2.5	$\langle \bar{B}_i B'_j v'_{i,j} \rangle$	-1.8
$\langle \mathcal{S}_{B'} \rangle$	230	$-\langle \bar{B}_i v'_j B'_{i,j} \rangle$	-3.0
$\langle \mathcal{L}' \rangle$	-43.9	$-\langle \bar{B}_i B'_k v'_{k,k} \rangle$	-5.2
$\langle B'_i \bar{B}_j v'_{i,j} \rangle$	-3.6	$\langle F_{u_{\bar{B}}} \rangle$	-1.1
$-\langle B'_i v'_j \bar{B}_{i,j} \rangle$	7.9	$\left\langle \bar{v}_i \frac{\partial u_{\bar{B}}}{\partial x_i} \right\rangle$	0.18
$-\langle B'_i \bar{B}_k v'_{k,k} \rangle$	-5.2	$\langle D_{\bar{B}}^{\text{res}} \rangle$	-3.7
$\left\langle \bar{v}_j \frac{\partial u_{B'}}{\partial x_j} \right\rangle$	-1.4		
$\langle D_{B'}^{\text{res}} \rangle$	-180		
Poynting flux		Turbulent Poynting flux	
$\langle F_{\mathcal{P}} \rangle$	-27.6	$\langle F_{\mathcal{P}'} \rangle$	-1.1
$\langle F_{\mathcal{P}-r} \rangle$	-9.2	$\langle F_{\mathcal{P}'-r} \rangle$	0.1
$\langle F_{\mathcal{P}-\theta} \rangle$	-18.4	$\langle F_{\mathcal{P}'-\theta} \rangle$	-1.2
$\langle F_{\mathcal{P}-\text{Adv}} \rangle$	-3.3	$\langle F_{\mathcal{P}'-\text{Adv}} \rangle$	-0.5
$\langle F_{\mathcal{P}-\text{Stress}} \rangle$	-24.3	$\langle F_{\mathcal{P}'-\text{Stress}} \rangle$	-0.6
Turbulent kinetic energy		Internal energy	
$\langle \dot{u}_{K'} \rangle$	$0.041 \pm 0.38$	$\langle \dot{u}_{\epsilon} \rangle$	$3.3 \pm 3.1$
$\langle \mathcal{S}_{K'} \rangle$	88.1	$\langle F_{u_{\epsilon}} \rangle$	-32.4
$-\langle \mathcal{L}' \rangle$	43.9	$\langle F'_{u_{\epsilon}} \rangle$	7.66
$\langle F'_{K'} \rangle$	-0.5	$-\langle p v'_{k,k} \rangle$	48.1
$\langle F_{K'} \rangle$	0.4	$-\langle p \bar{v}_{k,k} \rangle$	-22.3
$\langle v'_i B'_j \bar{B}_{i,j} \rangle$	1.9	$\langle D^{\text{rad}} \rangle$	-177
$-\langle v'_i \frac{\partial p}{\partial x_i} \rangle$	-46.4	$\langle D^{\epsilon} \rangle$	180
$\langle D_{B'}^{\text{visc}} \rangle$	-87.4		

energy input term is a correlation between the mean field Maxwell stress and the mean flow shear ( $\langle \mathcal{S}_{\bar{B}} \rangle$  - Eq 38). Energy is primarily removed via dissipation ( $D_{\bar{B}}^{\text{res}}$ ). It is interesting to note that terms involving turbulent fields only appear to play a role in removing mean magnetic energy. For instance, terms related to turbulent magnetic field line stretching ( $-\langle \bar{B}_i v'_j B'_{i,j} \rangle$ ) and expansions in the turbulent velocity field ( $-\langle \bar{B}_i B'_k v'_{k,k} \rangle$ ) remove comparable amounts of mean magnetic energy to dissipation. Compressibility is not negligible, consistent with the findings of Gardiner & Stone (2005b), Johansen et al. (2009), and Parkin & Bicknell (2013b). This feature may be linked to large scale spiral density waves (e.g. Heinemann & Papaloizou 2009, 2012) which can be seen in snapshots of the simulation.

In summary, based on an analysis of the turbulent (§ 4.1) and mean magnetic energies, the main input to turbulent magnetic energy comes from correlations between turbulent terms. Moreover, terms featuring mean-turbulent field correlations remove mean magnetic energy, thus acting like a turbulent resistivity. The interaction between mean

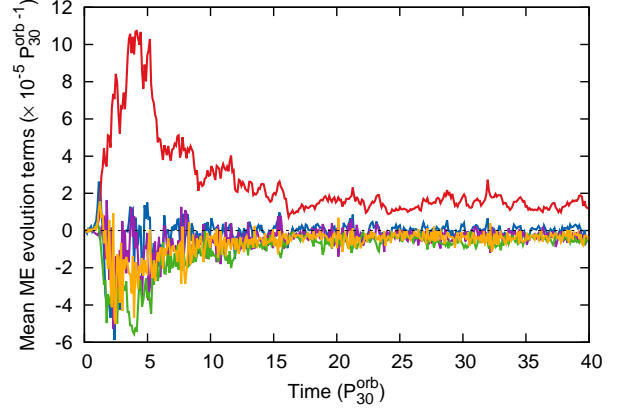


**Figure 8.** Mean magnetic energy evolution (see § 4.2). Shown are:  $\langle \dot{u}_{\bar{B}} \rangle$  (blue),  $\langle \mathcal{S}_{\bar{B}} \rangle$  (red),  $-\langle \bar{B}_i v'_j B'_{i,j} \rangle$  (purple),  $-\langle \bar{B}_i B'_k v'_{k,k} \rangle$  (green), and  $\langle D_{\bar{B}}^{\text{res}} \rangle$  (orange). Positive values indicate energy input, whereas negative values indicate removal of energy.

and turbulent fields, and the resulting influence on the evolution and maintenance of turbulence in the disk, are only weakly apparent. In the following section we turn to the mean field induction equation for further details of mean-turbulent field interactions.

### 4.3 Mean field induction equation

In our analysis, the turbulent magnetic fields are deviations from time-dependent mean magnetic fields. Hence, although mean magnetic fields do not feature in the largest terms in the turbulent magnetic energy equation, their importance is implicit in the time-dependent evolution of the turbulent magnetic field. In this section we examine the mean magnetic field induction equation, which exhibits a clear interplay between mean and turbulent fields.

#### 4.3.1 Volume averaged form

The volume-averaged mean field induction equation is,

$$\frac{\partial}{\partial t} \langle B_i \rangle = -\langle (\nabla \times \bar{\mathcal{E}})_i \rangle - \langle (\nabla \times \mathcal{E}')_i \rangle \quad (41)$$

where  $\bar{\mathcal{E}}_i = \epsilon_{ijk} \bar{v}_j \bar{B}_k$  and  $\mathcal{E}'_i = \epsilon_{ijk} v'_j B'_k$  are the mean and turbulent electromotive force (EMF), respectively. Note that we have neglected to include a numerical resistive term in this analysis - there is little indication from the results that it plays a considerable role in magnetic field induction.

From Fig. 9 one can see that the contributions to mean field evolution are complex. The results are, however, suggestive of quasi-periodic oscillations, and more so for the azimuthal induction equation compared to the radial equation. From the upper panel of Fig. 9 the evolution of  $\langle B_r \rangle$  is more strongly correlated with the turbulent EMF, with a secondary influence from the mean EMF. The weak influence of the mean EMF on  $\frac{\partial}{\partial t} \langle B_r \rangle$  arises from our azimuthal averaging of the mean fields, which defines them as axisymmetric, making,

$$\langle (\nabla \times \bar{\mathcal{E}})_r \rangle = \frac{1}{r \sin \theta} \frac{\partial \bar{\mathcal{E}}_\phi}{\partial \theta}, \quad (42)$$

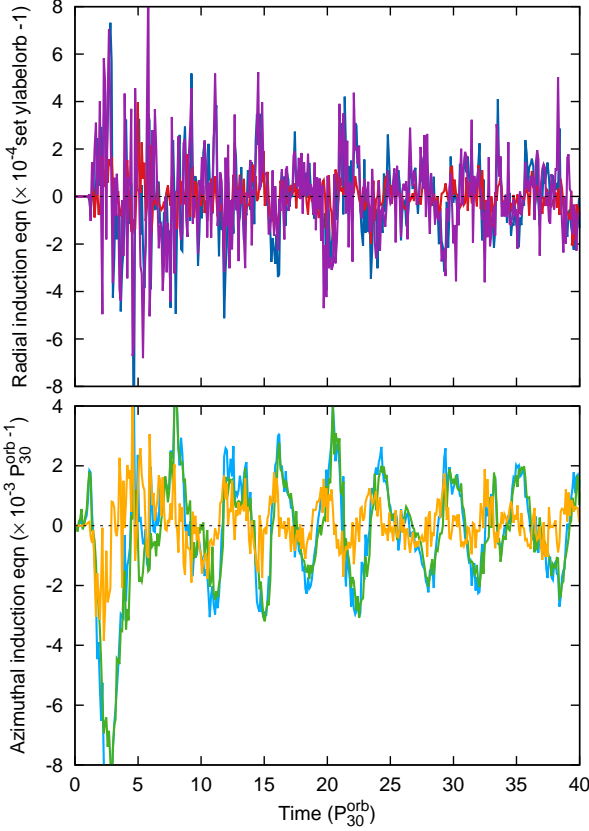


**Figure 9.** Volume integrated mean field induction equations for  $\langle B_r \rangle$  (upper) and  $\langle B_\phi \rangle$  (lower). Shown are:  $\frac{\partial}{\partial t} \langle B_r \rangle$  (dark blue),  $-\langle (\nabla \times \bar{\mathcal{E}})_r \rangle$  (red),  $-\langle (\nabla \times \mathcal{E}')_r \rangle$  (purple),  $\frac{\partial}{\partial t} \langle B_\phi \rangle$  (light blue),  $-\langle (\nabla \times \bar{\mathcal{E}})_\phi \rangle$  (green), and  $-\langle (\nabla \times \mathcal{E}')_\phi \rangle$  (orange).

where  $\bar{\mathcal{E}}_\phi = \bar{v}_\theta \bar{B}_r - \bar{v}_r \bar{B}_\theta$ . Hence, because  $\bar{B}_\theta$  and  $\bar{v}_\theta$  are relatively small, and vertical gradients in these quantities are reasonably flat below  $|z| < 2H$  (Fig. 2), one finds  $\langle (\nabla \times \bar{\mathcal{E}})_r \rangle$  to be small. In contrast, for  $\langle B_\phi \rangle$  (lower panel) the mean EMF is the main driver with a minor contribution from the turbulent EMF. In both cases, the weaker contributor (i.e. the mean EMF in the upper panel) is slightly out of phase, leading by roughly a quarter of an oscillation period.

#### 4.3.2 Induction at surfaces

The induction equation can also provide information about the role of different surfaces in the disk for mean magnetic field generation (Parkin & Bicknell 2013b). We write the azimuthal equation in contra-variant form as this exposes the importance of different surfaces for mean field generation. For the mean radial and azimuthal magnetic fields, with  $\mathcal{E} = \bar{\mathcal{E}} + \mathcal{E}'$ , one has,

$$\frac{\partial}{\partial t} \langle B_r \rangle = -\frac{1}{V} \int_{\theta_2} \mathcal{E}_\phi ds_\theta + \frac{1}{V} \int_{\theta_1} \mathcal{E}_\phi ds_\theta, \quad (43)$$

and,

$$\frac{\partial}{\partial t} \left\langle \frac{B_\phi}{r \sin \theta} \right\rangle = -\frac{1}{V} \int_{r_2} \frac{\mathcal{E}_\theta}{r \sin \theta} ds_r + \frac{1}{V} \int_{r_1} \frac{\mathcal{E}_\theta}{r \sin \theta} ds_r$$

$$-\frac{1}{V} \int_{\theta_2} \frac{\mathcal{E}_r}{r \sin \theta} ds_\theta + \frac{1}{V} \int_{\theta_1} \frac{\mathcal{E}_r}{r \sin \theta} ds_\theta, \quad (44)$$

where  $V = \iiint dV$  is the volume bound by the surfaces,  $ds_r = r^2 \sin \theta d\theta d\phi$ , and  $ds_\theta = r \sin \theta dr d\phi$ .

Only the vertical boundaries contribute to the evolution of  $\langle B_r \rangle$ ; the contribution from  $\partial \mathcal{E}'_\theta / \partial \phi$  drops out due to periodicity in the azimuthal direction. Hence, the disk-corona interface plays an intimate part in the generation of mean radial fields in the disk. This shows that the vertical component of the EMF cannot aid mean radial field evolution on the largest realizable scales<sup>4</sup> (see also the discussion in Brandenburg et al. 1995; Davis et al. 2010; Gressel 2010). Recalling that the turbulent EMF provides the dominant contribution to the evolution of  $\langle B_r \rangle$  (Fig. 9), there is a suggestion that buoyantly rising turbulent motions are crucial to mean radial field evolution (e.g. Tout & Pringle 1992). Previous studies have alluded to a crucial importance for the corona in driving the turbulence within the disk (e.g. Sorathia et al. 2010; Guan & Gammie 2011; Beckwith et al. 2011). The analysis in this subsection provides a natural explanation.

#### 4.3.3 A simple harmonic oscillator dynamo model

Magnetic field oscillations indicative of a mean field dynamo have been observed in a number of simulation studies of stratified disks (e.g. Brandenburg et al. 1995; Stone et al. 1996; Miller & Stone 2000; Arlt & Rüdiger 2001; Fromang & Nelson 2006; Davis et al. 2010; Gressel 2010; Shi et al. 2010; Guan & Gammie 2011; Simon et al. 2011; Oishi & Mac Low 2011; O'Neill et al. 2011; Flock et al. 2012a; Parkin & Bicknell 2013b). Inspecting the data from the simulation presented in this work, there is a striking correlation between  $\frac{\partial}{\partial t} \langle B_r \rangle$  with  $\langle B_\phi \rangle$ , and  $\frac{\partial}{\partial t} \langle B_\phi \rangle$  with  $\langle B_r \rangle$ . Brandenburg et al. (1995) observed similar behaviour, which led them to search for correlations between  $\langle \mathcal{E}'_\phi \rangle$  and  $\langle B_\phi \rangle$  as, since in the context of mean field dynamo theory (Krause & Raedler 1980), that would close a simple model for mean field evolution. Flock et al. (2012a) have repeated this exercise for global simulations, finding the same correlation. Indeed, our simulation results also exhibit an apparent  $\langle \mathcal{E}'_\phi \rangle \propto \langle B_\phi \rangle$  relation. The physical picture indicated by these relations is the one of creation of mean toroidal field from radial field via shear, combined with vertical gradients in  $\langle \mathcal{E}'_\phi \rangle$  converting toroidal field into radial field. The latter mechanism is indirect in the sense that  $\langle B_\phi \rangle$  does not explicitly feature in  $\langle \mathcal{E}'_\phi \rangle$ . Hence, an intermediate agent, related to the turbulent fields and in the vertical direction, must operate. Buoyant motions (e.g. Parker instability - Tout & Pringle 1992) and/or the non-axisymmetric MRI (Balbus & Hawley 1992; Terquem & Papaloizou 1996) seem viable. These points are discussed further by, for example, Brandenburg et al. (1995), Brandenburg (2005), Davis et al. (2010), Gressel (2010), Oishi & Mac Low (2011), and Flock et al. (2012a).

In the following we consider the basic dynamo model outlined above, which we cast as:

<sup>4</sup> Davis et al. (2010) do, however, find evidence for  $\partial \mathcal{E}'_\theta / \partial \phi$  being important for a small scale dynamo with the implication that non-axisymmetric perturbations drive energy evolution on the smallest scales.

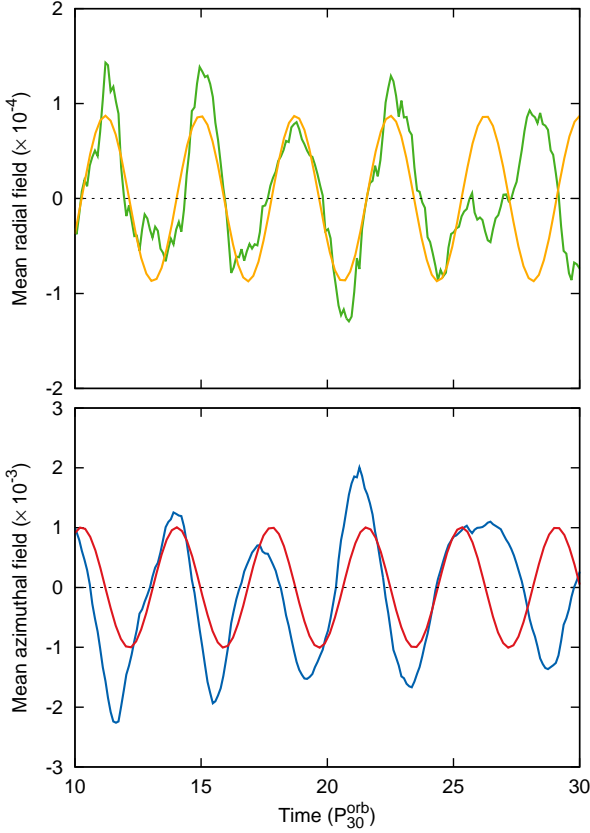


**Figure 10.** Comparing the basic dynamo model to the simulation data for the radial (upper panel) and azimuthal (lower panel) magnetic fields (see § 4.3.3). Shown are:  $\langle B_r \rangle$  from the simulation data (green), the model  $\langle B_r \rangle$  given by Eq (47) (orange),  $\langle B_\phi \rangle$  from the simulation data (blue), and the model  $\langle B_\phi \rangle$  given by Eq (48) (red).

$$\frac{\partial}{\partial t} \langle B_r \rangle = \frac{1}{\tau_{\text{turb}}} \langle B_\phi \rangle, \quad (45)$$

and,

$$\frac{\partial}{\partial t} \langle B_\phi \rangle = \left\langle \frac{d\Omega}{d \ln r} \right\rangle \langle B_r \rangle, \quad (46)$$

where  $\langle d\Omega/d \ln r \rangle$  is the mean shear in the disk and  $\tau_{\text{turb}}$  is a timescale related to an undisclosed physical mechanism which allows the turbulence to regenerate radial field from toroidal field. Equations (45) and (46) describe the mean field evolution as a simple harmonic oscillator, affording the solution:

$$\langle B_r \rangle = -\omega \left\langle \frac{d\Omega}{d \ln r} \right\rangle^{-1} \langle B_\phi \rangle_0 \sin \omega t + \langle B_r \rangle_0 \cos \omega t, \quad (47)$$

and,

$$\langle B_\phi \rangle = \langle B_\phi \rangle_0 \cos \omega t + \left\langle \frac{d\Omega}{d \ln r} \right\rangle \omega^{-1} \langle B_r \rangle_0 \sin \omega t, \quad (48)$$

where  $\omega = (-\tau_{\text{turb}}^{-1} \langle d\Omega/d \ln r \rangle)^{1/2}$  is the oscillation frequency, and  $\langle B_r \rangle_0$  and  $\langle B_\phi \rangle_0$  are the volume averaged radial and azimuthal magnetic fields at time  $t = 0$ . Note that  $\omega$  is real so long as the angular velocity decreases as a function of radius. This is satisfied in a Keplerian disk and is a pre-

requisite for the MRI (Balbus & Hawley 1991). Furthermore, the dynamo period,

$$\tau_{\text{dyn}} = \frac{2\pi}{\omega} = 2\pi \left( \frac{-1}{\tau_{\text{turb}}} \left\langle \frac{d\Omega}{d \ln r} \right\rangle \right)^{-1/2}, \quad (49)$$

is a function of the mean shear in the disk,  $\langle d\Omega/d \ln r \rangle$ , and the turbulent timescale,  $\tau_{\text{turb}}$ . Comparing the basic model mean fields against the simulation data shows good agreement (Fig. 10), with  $\tau_{\text{dyn}} \simeq 3.8 P_{30}^{\text{orb}}$ . The corresponding turbulent timescale,  $\tau_{\text{turb}} \simeq 7 P_{30}^{\text{orb}}$ , is consistent with the growth time for a low wavenumber non-axisymmetric MRI mode seeded from a (mean) toroidal magnetic field (Balbus & Hawley 1992; Parkin & Bicknell 2013a). The model mean fields begin to diverge from the simulation data after an interval of roughly  $15 P_{30}^{\text{orb}}$ . This likely arises as a result of additional physics not included in Eqs (45) and (46). For example, a weaker intermittent secondary dynamo connected with the longer timescale oscillations in  $\langle B_\theta \rangle$  (see figure 11 of Parkin & Bicknell 2013b).

In summary, the induction equation provides insight into turbulent fields influencing mean field evolution. A prime site for grasping this interaction is in the mechanism(s) which allow the turbulent fields to regenerate mean radial field from, presumably, mean toroidal field. In the analysis above we have encapsulated this, potentially vast, complexity in a single parameter,  $\tau_{\text{turb}}$ . Ultimately, unlocking the underlying physics requires a more complete closure model (e.g. Ogilvie 2003; Pessah et al. 2006; Lesur & Ogilvie 2008) and/or a derivation of tensorial dynamo coefficients (Brandenburg 2005; Gressel 2010).

#### 4.4 Poynting flux

Models of Seyfert galaxy coronae typically invoke the presence of a hot coronal region overlying a cool disk (commonly known as “reflection” models - Haardt & Maraschi 1991, 1993; Field & Rogers 1993). An important ingredient in these models is the fraction of energy transported to, and dissipated within, the coronal region. Hence, knowledge of the means by which a turbulent accretion disk transports energy into the coronal region is pivotal for accurate modelling.

The transport of electromagnetic energy through the boundaries of the accretion disk can be assessed using the Poynting flux. Our main focus will be on the directional contributions, and later, the stress-related and advection-related components of the total Poynting flux. Taking the scalar product of  $B_i$  with the induction equation (written in a conservative form), then averaging the resulting equation over a volume,  $V$ , with bounding surface,  $s$ , one has:

$$\frac{\partial}{\partial t} \langle u_B \rangle = \langle F_P \rangle + \langle (B_i v_j - v_i B_j) B_{i;j} \rangle, \quad (50)$$

where the Poynting vector,  $\mathcal{P}$ , is given by Eq (27), and the volume-averaged total Poynting flux is,

$$\langle F_P \rangle = -\frac{1}{V} \int \nabla \cdot \mathcal{P} dV = -\frac{1}{V} \int_s \mathcal{P}_j ds_j. \quad (51)$$

Fig. 11 shows the evolution of the Poynting flux in the simulation. During the initial transient evolution of the simulation, there is a large influx of magnetic energy in the radial direction. As the evolution of the disk proceeds, the positive



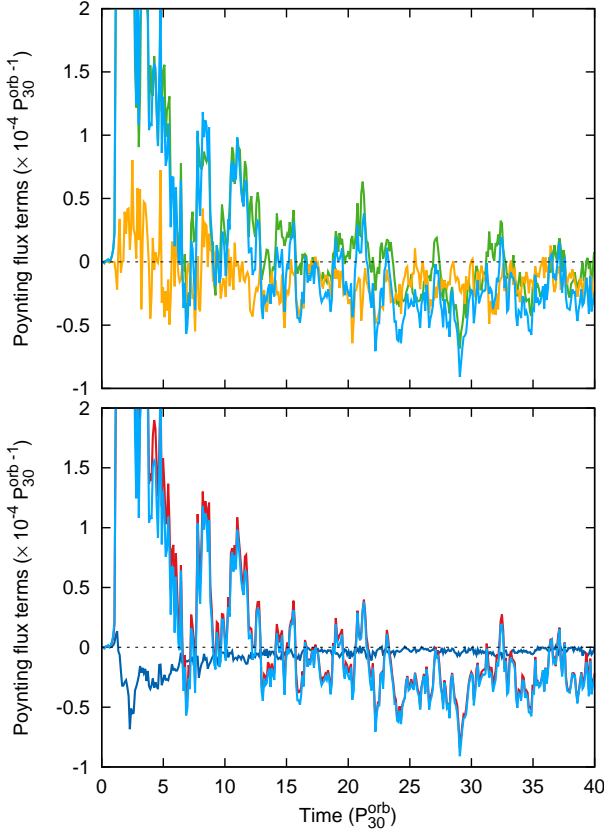


**Figure 11.** The Poynting flux evaluated from the simulation data (see § 4.4). The analysis was performed over the region  $15 < r < 25$  and  $|z| \leq 2H$ . In the upper panel the radial ( $\langle F_{\mathcal{P}-r} \rangle$  - green), vertical ( $\langle F_{\mathcal{P}-\theta} \rangle$  - orange), and total ( $\langle F_{\mathcal{P}} \rangle$  - light blue) contributions to the Poynting flux are plotted. The lower panel shows the contributions from the stress-related ( $\langle F_{\mathcal{P}-\text{Stress}} \rangle$  - red) and advection-related ( $\langle F_{\mathcal{P}-\text{Adv}} \rangle$  - dark blue) parts of the Poynting flux. Positive values indicate an influx of magnetic energy into the disk, and vice-versa for negative values. Corresponding time-averaged values are noted in Table 3.

contribution from the radial boundaries subsides and the total Poynting flux becomes dominated by an outwardly directed flux through the vertical boundaries (Table 3). Thus, once the quasi-steady turbulent state is reached, the Poynting flux mostly acts to transfer magnetic energy from the disk body ( $|z| \leq 2H$ ) into the coronal region ( $|z| > 2H$ ).

The contribution to the Poynting flux from advection of electromagnetic energy is small. One can see this by considering the second equality for the Poynting vector in Eq (27), where the separate contributions due to advection of magnetic energy ( $\propto u_B v_j$ ) and Maxwell stresses ( $\propto v_i M_{ij}$ ) are more clear. Defining,

$$\langle F_{\mathcal{P}-\text{Adv}} \rangle = -\frac{1}{V} \int_{\mathcal{V}} u_B v_j ds_j, \quad (52)$$

and,

$$\langle F_{\mathcal{P}-\text{Stress}} \rangle = -\frac{1}{V} \int_{\mathcal{V}} v_i M_{ij} ds_j, \quad (53)$$

it is evident from the lower panel of Fig. 11 that the majority

of magnetic energy is carried away by the stress-related part of the total Poynting flux.

Shearing-box studies of wind-launching by MRI-active disks indicate<sup>5</sup> that it is the conversion of turbulent magnetic energy (carried by the turbulent Poynting flux) into kinetic energy which initiates the outflow (Suzuki & Inutsuka 2009; Suzuki et al. 2010; Io & Suzuki 2013). In this case the advection-related and stress-related components of the *turbulent* Poynting flux are found to be comparable. We have not witnessed wind launching in the simulation presented in this work. This does not seem to be due to the simulation transporting an insufficient amount of energy into the coronae via the turbulent Poynting flux as values for  $\langle F_{\mathcal{P}'} \rangle$  (and its various components) noted in Table 3 are in good agreement with recent global simulations by Suzuki & Inutsuka (2013), namely  $\langle F_{\mathcal{P}'-\text{Adv}} \rangle \sim \langle F_{\mathcal{P}'-\text{Stress}} \rangle$ . (It should, however, be noted that the turbulent Poynting flux is significantly smaller than the total Poynting flux,  $|\langle F_{\mathcal{P}'} \rangle| \ll |\langle F_{\mathcal{P}} \rangle|$ .) Possible explanations for the lack of wind launching in the simulation are an insufficient vertical extent to the domain or, as discussed in § 3, the reflection of waves off the boundaries inhibiting vertical motion.

To put the importance of the Poynting flux to magnetic field evolution into context, the total Poynting flux,  $\langle F_{\mathcal{P}} \rangle$ , removes roughly 11% of the total generated magnetic energy ( $\sim \langle S_{B'} \rangle + \langle S_{\bar{B}} \rangle$  - see Table 3), with roughly 8% going into the corona via  $\langle F_{\mathcal{P}-\theta} \rangle$ . These results disagree with Miller & Stone (2000), who inferred that  $\sim 25\%$  of the magnetic energy produced in the disk body is transported to the corona. There are, however, substantial differences between the numerical setup and methods of analysis used by Miller & Stone (2000) and ourselves, which could account for some of this difference. Nonetheless, there is a very important difference in the physical mechanism posited to drive magnetic energy into the corona. Miller & Stone (2000) attribute buoyant rising of flux tubes, whereas the results in Fig. 11 and Table 3 suggest that it is in fact the stress like part of the Poynting flux, not buoyant advection, that plays the prominent role. This finding has important implications for models of coronal powering, as discussed at the beginning of this section.

#### 4.5 Turbulent kinetic energy evolution

The turbulent kinetic energy provides an insight into the energy possessed by velocity fluctuations that are effectively carried along by the mean rotation. In this regard, when considering an analysis in the inertial frame, it is essential to separate turbulent and mean velocities. The derivation of the turbulent kinetic energy equation begins with the momentum equation (Eq 2) with a term added to account for numerical viscous losses,  $d^{\text{visc}}$ ,

$$\frac{\partial \rho v_i}{\partial t} + \frac{\partial}{\partial x_j} (\rho v_i v_j) = -\rho \frac{\partial \Phi}{\partial x_i} - \frac{\partial p}{\partial x_i} + \frac{\partial M_{ij}}{\partial x_j} + d_i^{\text{visc}}. \quad (54)$$

The velocity and magnetic fields are then decomposed into mean and turbulent components (§ 2.4), the scalar prod-

<sup>5</sup> However, many properties of the wind-launching follow the standard picture of magnetocentrifugal winds (Blandford & Payne 1982; Ogilvie 2012; Fromang et al. 2013; Lesur et al. 2013; Bai & Stone 2013).

uct with  $v'_i$  is taken, and the resulting equation is Reynolds averaged. The term containing the Maxwell stress may be expanded as follows,

$$\overline{v'_i \frac{\partial M_{ij}}{\partial x_j}} = \overline{v'_i \frac{\partial M'_{ij}}{\partial x_j}} + \overline{v'_i B'_j \frac{\partial \bar{B}_i}{\partial x_j}}, \quad (55)$$

where  $M'_{ij}$  is the turbulent Maxwell stress tensor (§ 4.1). The azimuthally-averaged turbulent kinetic energy equation then reads,

$$\begin{aligned} \frac{\partial \overline{u_{K'}}}{\partial t} = & -\overline{\rho v'_i v'_j \bar{v}_{i,j}} - \frac{\partial}{\partial x_j} (\overline{u_{K'} \bar{v}_j}) - \frac{\partial}{\partial x_j} (\overline{u_{K'} v'_j}) \\ & + \overline{v'_i \frac{\partial M'_{ij}}{\partial x_j}} + \overline{v'_i B'_j \bar{B}_{i,j}} - \overline{v'_i \frac{\partial p}{\partial x_i}} + \overline{v'_i d_i^{\text{visc}}}, \end{aligned} \quad (56)$$

where  $u_{K'} = \frac{1}{2} \rho |v'|^2$  is the turbulent kinetic energy. Finally, we take an average of Eq (56) over a meridional ( $r, \theta$ ) plane, which leads to a volume averaged turbulent kinetic energy equation (see Eq 18):

$$\begin{aligned} \langle \dot{u}_{K'} \rangle = & \langle \mathcal{S}_{K'} \rangle + \langle F'_{K'} \rangle + \langle F_{K'} \rangle - \langle \mathcal{L}' \rangle + \langle v'_i B'_j \bar{B}_{i,j} \rangle \\ & - \left\langle v'_i \frac{\partial p}{\partial x_i} \right\rangle + \langle D^{\text{visc}} \rangle, \end{aligned} \quad (57)$$

with the symbols defined as,

$$\langle \dot{u}_{K'} \rangle = \frac{\partial}{\partial t} \langle u_{K'} \rangle, \quad (58)$$

$$\langle \mathcal{S}_{K'} \rangle = -\langle \rho v'_i v'_j \bar{v}_{i,j} \rangle, \quad (59)$$

$$\langle F'_{K'} \rangle = -\left\langle \frac{\partial}{\partial x_j} (u_{K'} v'_j) \right\rangle = -\frac{1}{V} \int_s u_{K'} v'_j ds_j, \quad (60)$$

$$\langle F_{K'} \rangle = -\left\langle \frac{\partial}{\partial x_j} (u_{K'} \bar{v}_j) \right\rangle = -\frac{1}{V} \int_s u_{K'} \bar{v}_j ds_j, \quad (61)$$

$$\langle D^{\text{visc}} \rangle = \langle v'_i d_i^{\text{visc}} \rangle. \quad (62)$$

The energy removed by (numerical) viscous dissipation is accounted for by the term  $\langle D^{\text{visc}} \rangle$ . Note that the value of  $\langle D^{\text{visc}} \rangle$  is evaluated as the remainder required to balance Eq (57), as all other terms may be computed explicitly. As with the term  $\langle D_{B'}^{\text{res}} \rangle$  in the magnetic energy analysis, the advantage of this approach is that we can quantify dissipation without the need to ascribe to it a specific functional form. Time-averaged values for all of the terms in Eq (57) are noted in Table 3, with the evolution of the largest terms plotted in Fig. 12.

Turbulent kinetic energy input mainly comes from the interaction of the Reynolds stress with shear in the mean velocity field ( $\langle \mathcal{S}_{K'} \rangle$ ). Second to this is the contribution due to turbulent Lorentz forces,  $-\langle \mathcal{L}' \rangle$ . We recall that  $+\langle \mathcal{L}' \rangle$  was responsible for a removal of turbulent magnetic energy (see § 4.1 and Fig. 7), thus it embodies the majority of turbulent kinetic energy input directly due to the magnetized turbulence in the disk. Turning next to the energy removal, one sees from Fig. 12 that (numerical) viscous dissipation is the largest sink, followed by the term  $\langle v'_i \frac{\partial p}{\partial x_i} \rangle$ , which represents the work done on the turbulent fluctuations by the pressure force. In common with the turbulent magnetic energy analysis in § 4.1, we find that advection of turbulent kinetic energy in/out of the disk (the terms  $\langle F'_{K'} \rangle$  and  $\langle F_{K'} \rangle$ ) does little to the global energy budget when compared to in-situ generation and dissipation (see Table 3).

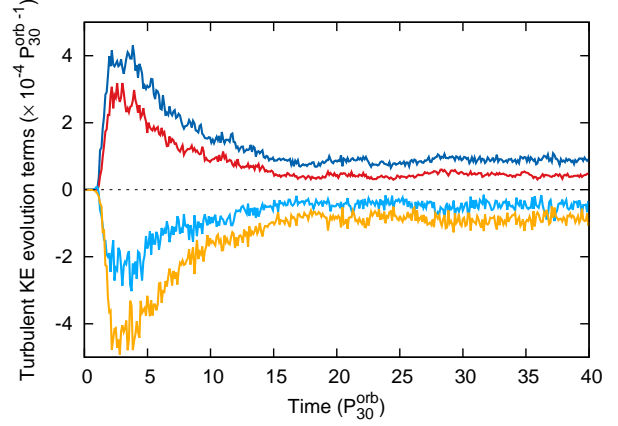


**Figure 12.** Terms pertaining to the evolution of the turbulent kinetic energy (§ 4.5). Shown are:  $\langle \mathcal{S}_{K'} \rangle$  (dark blue),  $-\langle \mathcal{L}' \rangle$  (red),  $-\langle v'_i \frac{\partial p}{\partial x_i} \rangle$  (light blue), and  $\langle D^{\text{visc}} \rangle$  (orange). Positive values indicate energy input, whereas negative values indicate removal of energy.

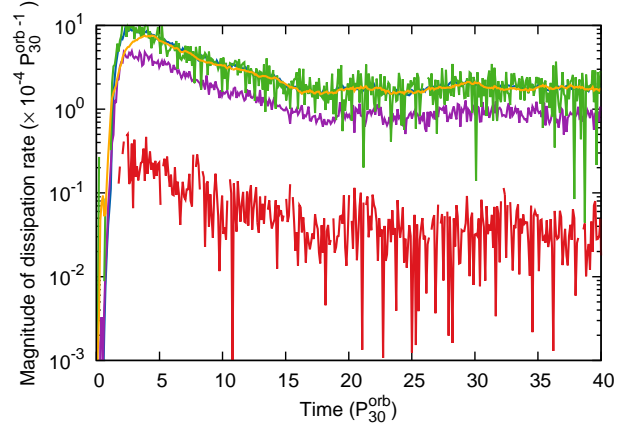


**Figure 13.** Comparing the various dissipation, heating, and cooling terms: turbulent resistive dissipation,  $\langle D_{B'}^{\text{res}} \rangle$  (blue); mean resistive dissipation,  $\langle D_B^{\text{res}} \rangle$  (red); viscous dissipation,  $\langle D^{\text{visc}} \rangle$  (purple); heating,  $\langle D_\epsilon \rangle$  (green); and cooling,  $\langle D_{\text{rad}} \rangle$  (orange). The curves for  $\langle D_{B'}^{\text{res}} \rangle$ ,  $\langle D_\epsilon \rangle$ , and  $\langle D_{\text{rad}} \rangle$  are closely coincident on the plot. Corresponding time-averaged values can be found in Table 3.

#### 4.6 Internal energy evolution

To complete the picture of energy flow through our model disk we now examine the internal energy equation. The volume-averaged equation is:

$$\langle \dot{u}_\epsilon \rangle = \langle F_{u_\epsilon} \rangle + \langle F'_{u_\epsilon} \rangle - \langle p v'_{k,k} \rangle - \langle p \bar{v}_{k,k} \rangle + \langle D^{\text{rad}} \rangle + \langle D^\epsilon \rangle, \quad (63)$$

where,

$$\langle \dot{u}_\epsilon \rangle = \frac{\partial}{\partial t} \langle u_\epsilon \rangle, \quad (64)$$

$$\langle F_{u_\epsilon} \rangle = -\frac{1}{V} \int_s u_\epsilon \bar{v}_j ds_j, \quad (65)$$

$$\langle F'_{u_\epsilon} \rangle = -\frac{1}{V} \int_s u_\epsilon v'_j ds_j. \quad (66)$$

Thermal energy is extracted by the cooling function, from which we define an associated radiative loss rate:

$$\langle D^{\text{rad}} \rangle = -\langle \rho \Lambda(T) \rangle, \quad (67)$$

where  $\Lambda(T)$  is the cooling function which is used to drive the temperature distribution in the disk towards that of the initial conditions. The term  $\langle D_\epsilon \rangle$  represents numerical heating - it takes its value from the remainder required to balance Eq (63). Time-averaged values for the terms in Eq (63) are noted in Table 3.

Compressibility is important for the internal energy evolution, with the compression-related terms  $-\langle \rho v'_{k,k} \rangle$  and  $-\langle \rho \bar{v}_{k,k} \rangle$  having appreciable values (Table 3). A significant amount of energy is also advected through the disk boundaries by the mean flow ( $\langle F_{u\epsilon} \rangle$ ).

Numerical heating ( $\langle D^\epsilon \rangle$ ) provides the largest source of internal energy in the disk. Importantly, as we are using an ideal MHD simulation, this shows that the energy being dissipated both resistively and viscously by the numerics is being effectively thermalized. Moreover, a comparison of the terms in Eq (63) (see Table 3), in particular  $\langle D^\epsilon \rangle$  and  $\langle D^{\text{rad}} \rangle$ , reveals that some of the thermalized energy is redirected into other terms, and is not entirely radiated away. This contrasts with the standard view of accretion disks, whereby the dissipation rates are directly equated to the radiative emission rate (e.g. Shakura & Sunyaev 1973). The deviation is, however, only minor, as illustrated by a comparison of dissipation, heating, and cooling rates in Fig. 13. Of course, the description of thermodynamics in our models is relatively simple, and a more rigorous understanding of the flow of internal energy requires a similar analysis to be applied to simulations using a more realistic treatment of radiation and cooling (Turner et al. 2003; Hirose et al. 2006; Ohsuga & Mineshige 2011; Blaes et al. 2011; Jiang et al. 2013; Flock et al. 2013). We compare our derived dissipation rates to previous work in § 5.2.

## 5 DISCUSSION

### 5.1 Global energy flow

Using the values for energy production and dissipation, and the energy exchange between turbulent magnetic and kinetic reservoirs, one can construct a simplified energy flow diagram, which is shown in Fig. 14. This starts with differential rotation (shear) in the mean rotation profile, which was shown in § 3 to be essentially Keplerian, and thus directly linked to the gravitational potential energy. Hence, the energy source for the largest components in the shear-stress correlations for turbulent magnetic ( $\mathcal{S}_{B'}$ ) and kinetic ( $\mathcal{S}_{K'}$ ) energies can be directly connected to Keplerian shear - see also the discussion in Brandenburg et al. (1995), Balbus & Hawley (1998), and Kuncic & Bicknell (2004). One can write the largest contributions to these terms as,

$$\langle \mathcal{S}_{B'} \rangle \approx \left\langle B'_\phi B'_r \left( \frac{\partial v_{\text{Kep}}}{\partial r} - \frac{v_{\text{Kep}}}{r} \right) \right\rangle = \left\langle B'_\phi B'_r \frac{d\Omega_{\text{Kep}}}{d \ln r} \right\rangle, \quad (68)$$

and,

$$\langle \mathcal{S}_{K'} \rangle \approx - \left\langle \rho v'_\phi v'_r \left( \frac{\partial v_{\text{Kep}}}{\partial r} - \frac{v_{\text{Kep}}}{r} \right) \right\rangle = - \left\langle \rho v'_\phi v'_r \frac{d\Omega_{\text{Kep}}}{d \ln r} \right\rangle, \quad (69)$$

where  $\Omega_{\text{Kep}} = v_{\text{Kep}}/r$ . Combining equations (68) and (69) yields the well-known correlation between the total stress tensor and shear in the the background/mean rotation profile:

$$\langle \mathcal{S}_{B'} \rangle + \langle \mathcal{S}_{K'} \rangle \approx - \left\langle \mathcal{T}_{r\phi} \frac{d\Omega_{\text{Kep}}}{d \ln r} \right\rangle, \quad (70)$$

where  $\mathcal{T}_{r\phi} = \rho v'_r v'_\phi - B'_r B'_\phi$  is the  $r - \phi$  component of the total turbulent stress tensor. As discussed by Balbus & Hawley (1998), the energy input contributed by the above, in combination with effective angular momentum transport, is at the heart of self-sustaining MHD turbulence in accretion disks.

Subsequent energy exchange between turbulent magnetic and kinetic energies largely occurs as a result of turbulent Lorentz forces,  $\mathcal{L}'$ . Hence, the turbulent kinetic energy receives  $\sim 1/3$  of its power from  $\mathcal{L}'$ . Energy flow ends with dissipation, and we can account for resistive and viscous dissipation with  $\langle D_{B'}^{\text{res}} \rangle$  and  $\langle D^{\text{visc}} \rangle$ , respectively.

There are a number of similarities, and some important differences between Fig. 14 and the energy flow chart presented by Brandenburg et al. (1995). Firstly, we agree that Keplerian shear is the main source of energy, consistent with the expectation for MRI driven turbulence (Balbus & Hawley 1992). Also, we find agreement that essentially all energy extracted from Keplerian shear is dissipated within the disk. However, our results indicate that turbulent kinetic energy extracts most of its power from Keplerian rotation, in contrast to Brandenburg et al. (1995) who inferred that the majority of power came from turbulent magnetic energy, with only  $\sim 1/3$  being drawn from Keplerian shear<sup>6</sup>. The origin of this difference is not clear as a comparison of energy generation terms indicates similar results. For instance, in the analysis by Brandenburg et al. (1995),  $\mathcal{S}_{K'} \sim 3/2\Omega_0 \langle \rho v_x v_y \rangle$  and  $\mathcal{S}_{B'} \sim -3/2\Omega_0 \langle B_x B_y \rangle$  (in cgs units, and where  $x$  and  $y$  are the radial and azimuthal shearing-box coordinates and  $\Omega_0$  is the angular velocity of the box centre), such that the ratio of energy injection terms is equivalent to the Maxwell-to-Reynolds stress ratio,  $\mathcal{S}_{B'}/\mathcal{S}_{K'} \equiv -\langle B_x B_y \rangle / \langle \rho v_x v_y \rangle$ . For model ‘‘A’’ from Brandenburg et al. (1995) - which includes a cooling term and is therefore a suitable candidate for comparison - a value of  $-\langle B_x B_y \rangle / \langle \rho v_x v_y \rangle \simeq 3.6$  is noted. For the global disk analysis presented in this work,  $\mathcal{S}_{B'}/\mathcal{S}_{K'} = 2.61$  and  $-\langle B'_r B'_\phi \rangle / \langle \rho v'_r v'_\phi \rangle = 2.69$  (see Tables 1 and 3). (The minor difference between  $\mathcal{S}_{B'}/\mathcal{S}_{K'}$  and  $-\langle B'_r B'_\phi \rangle / \langle \rho v'_r v'_\phi \rangle$  due to components in the energy injection terms in addition to the  $r - \phi$  Reynolds/Maxwell stress.) Hence, the reasons for the disagreement in energy flow diagrams is not immediately apparent. A possible resolution would be to repeat the mean-field analysis presented in this work for a well-resolved stratified shearing-box. This is beyond the scope of the present work, but would be a useful subject for future studies.

In summary, 81% of the energy extracted from Keplerian shear in the disk body is dissipated; this is estimated from  $(\langle D_{B'}^{\text{res}} \rangle + \langle D_B^{\text{res}} \rangle + \langle D^{\text{visc}} \rangle) / (\langle \mathcal{S}_{B'} \rangle + \langle \mathcal{S}_B \rangle + \langle \mathcal{S}_{K'} \rangle)$ . This number is considerable, and indicates that the disk is very efficient at thermalizing kinetic and magnetic energy.

<sup>6</sup> Simon et al. (2009) have presented an analysis of energetics based on unstratified shearing-box models. However, due to uncertainties in their values at low wavenumbers (i.e. on the large spatial scales that are best described by the volume-averaged approach in this work) it is difficult to make more than a speculative comparison against their results. Nevertheless, the transfer function analysis presented by Simon et al. (2009) does suggest that Reynolds stresses are effective at injecting turbulent kinetic energy on large scales.

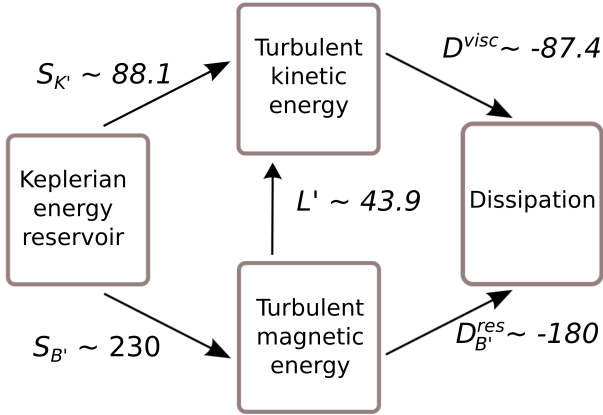


**Figure 14.** Energy flow diagram for turbulence in a global disk. All values are given in units of  $10^{-6} P_{30}^{\text{orb}-1}$  and have been volume averaged over the disk body and time averaged over the interval  $20 < t < 40 P_{30}^{\text{orb}}$ .

## 5.2 Comparison with previous studies

The vast majority of previous studies of energetics in a turbulent magnetized disk have utilised local (shearing-box) simulations. Here we compare and contrast those results against our findings from a global disk model. Our results agree well with those of Simon et al. (2009), who reported a viscous-to-resistive dissipation ratio,  $\langle D^{\text{visc}} \rangle / \langle D^{\text{res}} \rangle \simeq 0.5$  for unstratified shearing-box models with purely numerical dissipation, which should be compared with  $\langle D^{\text{visc}} \rangle / (\langle D_{B'}^{\text{res}} \rangle + \langle D_B^{\text{res}} \rangle) \simeq 0.48$  from this work. Making comparisons against dissipation rates for models which have included explicit diffusion coefficients is somewhat difficult and confusing. Miller & Stone (2000) found that resistive dissipation was 0.71% of viscous dissipation in their stratified disk models. In contrast, Brandenburg et al. (1995) note  $\langle D^{\text{visc}} \rangle / \langle D^{\text{res}} \rangle \simeq 4/3$ . One possible explanation for the difference between these two models would be that they have different effective magnetic Prandtl numbers,  $Pr_M = \nu/\eta$ , where  $\nu$  and  $\eta$  are viscosity and resistivity, respectively. In this regard, the models of Brandenburg et al. (1995) have  $Pr_M \sim 1$  if based on explicit diffusion coefficients, and  $Pr_M \sim 10$  if based on artificial viscosity coefficients. However, viscosity and resistivity values used by Miller & Stone (2000) are not given, complicating a comparison. In these somewhat earlier simulations of MRI-driven turbulence, the focus was less on the influence of the Prandtl number dependence of the turbulent dissipation, and more on exploring fundamental features of the turbulence. In recent years the focus has shifted somewhat, with a Prandtl number dependence to the turbulence having been revealed (Fromang et al. 2007; Lesur & Longaretti 2007; Longaretti & Lesur 2010; Simon et al. 2011; Käpylä & Korpi 2011; Oishi & Mac Low 2011). Examining the role of the Prandtl number in setting the dissipation rates in a global context is, therefore, an interesting avenue for future studies.

We have not defined a functional form for the numerical dissipation terms in this work. Indeed, the adopted analysis approach does not demand it. Numerical dissipation does not necessarily behave in the same manner as standard non-ideal dissipation. This point is discussed further by Xu & Li

(2001), Hirose et al. (2006), Fromang & Papaloizou (2007), Simon et al. (2009), Hawley et al. (2011), Parkin & Bicknell (2013b), and Salvesen et al. (2013). Nevertheless, if we assume an Ohmic form for  $\langle D_{B'}^{\text{res}} \rangle$ , and a Newtonian shear-stress form for  $\langle D^{\text{visc}} \rangle$ , we find a numerical magnetic Prandtl number,  $Pr_M \simeq 0.6$ . Although this does not agree exactly with the value of  $Pr_M \simeq 2$  estimated by Simon et al. (2009), both values are within a factor of two of unity. Considering that astrophysical objects are expected to span a wide range of values of  $Pr_M$  (Brandenburg & Subramanian 2005; Balbus & Henri 2008), deviating substantially from unity in many cases, further progress requires the consideration of explicitly non-ideal global models (e.g. Flock et al. 2012b).

## 6 CONCLUSIONS

The results of a high-resolution, three-dimensional, magnetohydrodynamic disk simulation have been used to evaluate the flow of energy, and detailed interactions between mean and turbulent fields, for MRI-driven turbulence in a global setting. To this end we have used a Reynolds averaged mean-field approach to study equations for: the turbulent magnetic energy, mean magnetic energy, mean field induction, turbulent kinetic energy, and internal energy. The results show that the correlation between turbulent Reynolds and Maxwell stresses with shear in the (almost Keplerian) mean rotation provides the main source of turbulent energy. Turbulent Lorentz forces extract magnetic energy and inject it into kinetic energy. Terms featuring the mean magnetic fields do not contribute significantly to the turbulent magnetic energy evolution. However, turbulent fields are fluctuations about a mean. As such, the indirect influence of mean magnetic fields on the turbulent magnetic energy can be understood from the mean magnetic field induction equation. For the case of the mean radial magnetic field the turbulent EMF is the primary driver, highlighting an example of turbulence driving the evolution of mean fields.

A number of interesting results have also been revealed regarding the Poynting flux. During the quasi-steady state of the simulation, the Poynting flux carries an amount of energy equating to 8% of the total magnetic energy input into the corona. This value is somewhat lower than estimates from previous shearing-box studies, although this could simply be the result of the different simulation setup and analysis methods used. More important, however, is the finding that the stress-related part of the Poynting flux is roughly seven times larger than the advection-related part, a result which has considerable importance for models of coronal powering in Seyfert galaxies that typically invoke buoyant rising of flux tubes for electromagnetic energy transport.

The basic picture for the disk “engine” painted by the results of the analysis in this work bears many similarities with findings from previous shearing-box studies: stress-shear terms power the turbulence with turbulent Lorentz forces providing a means of transporting energy between the magnetic and kinetic reservoirs, and all paths ending with dissipation. However, a number of important differences have been uncovered. Most striking is our finding that the turbulent kinetic energy is mostly fed from terms associated with Keplerian shear, and not by Lorentz forces, in contrast to the results of Brandenburg et al. (1995).



In closing we note that the control volume analysis utilised in this work provides spatially-averaged information about turbulent energetics. However, the power spectra presented in Fig. 6 indicate that the ordering of strengths in directional components of the turbulent fields changes between the very largest and smallest scales. Hence, with an eye to gaining further insight into the scale-dependence of energetics in a turbulent disk, and the possibility that the very smallest scales behave differently to the largest (energy containing) scales, it would be interesting to perform a follow-up analysis in wavenumber space.

### Acknowledgements

I thank Geoffrey Bicknell for numerous insightful discussions and the anonymous referee for a prompt and constructive report which helped to clarify points in the paper. This research was supported under the Australian Research Council's Discovery Projects funding scheme (project number DP1096417), and by NCI Facility at the ANU.

### REFERENCES

- Arlt, R. & Rüdiger, G. 2001, *A&A*, 374, 1035  
 Bai, X.-N. & Stone, J. M. 2013, *ApJ*, 767, 30  
 Balbus, S. A. & Hawley, J. F. 1991, *ApJ*, 376, 214  
 Balbus, S. A. & Hawley, J. F. 1992, *ApJ*, 400, 610  
 Balbus, S. A. & Hawley, J. F. 1998, *Reviews of Modern Physics*, 70, 1  
 Balbus, S. A. & Henri, P. 2008, *ApJ*, 674, 408  
 Beckwith, K., Armitage, P. J., & Simon, J. B. 2011, *MNRAS*, 416, 361  
 Blackman, E. G. & Pessah, M. E. 2009, *ApJL*, 704, L113  
 Blaes, O., Krolik, J. H., Hirose, S., & Shabaltas, N. 2011, *ApJ*, 733, 110  
 Blandford, R. D. & Payne, D. G. 1982, *MNRAS*, 199, 883  
 Brandenburg, A. 2005, *Astronomische Nachrichten*, 326, 787  
 Brandenburg, A., Nordlund, A., Stein, R. F., & Torkelsson, U. 1995, *ApJ*, 446, 741  
 Brandenburg, A. & Subramanian, K. 2005, *PhR*, 417, 1  
 Colella, P. & Woodward, P. R. 1984, *J. Comput. Phys*, 54, 174  
 Davidson, P. 2004, *Turbulence : An Introduction for Scientists and Engineers: An Introduction for Scientists and Engineers*. OUP Oxford  
 Davis, S. W., Stone, J. M., & Pessah, M. E. 2010, *ApJ*, 713, 52  
 Favre, A. 1969, in *Problems of hydrodynamics and continuum mechanics*. SIAM  
 Field, G. B. & Rogers, R. D. 1993, *ApJ*, 403, 94  
 Flock, M., Dzyurkevich, N., Klahr, H., Turner, N., & Henning, T. 2012a, *ApJ*, 744, 144  
 Flock, M., Dzyurkevich, N., Klahr, H., Turner, N. J., & Henning, T. 2011, *ApJ*, 735, 122  
 Flock, M., Fromang, S., González, M., & Commerçon, B. 2013, arXiv:1310.5865  
 Flock, M., Henning, T., & Klahr, H. 2012b, *ApJ*, 761, 95  
 Fromang, S., Latter, H., Lesur, G., & Ogilvie, G. I. 2013, *A&A*, 552, A71  
 Fromang, S. & Nelson, R. P. 2006, *A&A*, 457, 343  
 Fromang, S. & Papaloizou, J. 2007, *A&A*, 476, 1113  
 Fromang, S., Papaloizou, J., Lesur, G., & Heinemann, T. 2007, *A&A*, 476, 1123  
 Gardiner, T. A. & Stone, J. M. 2005a, *Journal of Computational Physics*, 205, 509  
 Gardiner, T. A. & Stone, J. M. 2005b, in de Gouveia dal Pino E. M., Lugones G., Lazarian A., eds, *Magnetic Fields in the Universe: From Laboratory and Stars to Primordial Structures*. Vol. 784 of AIP Conf. Ser. pp 475–488  
 Gombosi, T. I., Tóth, G., de Zeeuw, D. L., Hansen, K. C., Kabin, K., & Powell, K. G. 2002, *Journal of Computational Physics*, 177, 176  
 Gressel, O. 2010, *MNRAS*, 405, 41  
 Guan, X. & Gammie, C. F. 2011, *ApJ*, 728, 130  
 Haardt, F. & Maraschi, L. 1991, *ApJL*, 380, L51  
 Haardt, F. & Maraschi, L. 1993, *ApJ*, 413, 507  
 Hawley, J. F., Gammie, C. F., & Balbus, S. A. 1995, *ApJ*, 440, 742  
 Hawley, J. F., Guan, X., & Krolik, J. H. 2011, *ApJ*, 738, 84  
 Hawley, J. F., Richers, S. A., Guan, X., & Krolik, J. H. 2013, *ApJ*, 772, 102  
 Heinemann, T. & Papaloizou, J. C. B. 2009, *MNRAS*, 397, 64  
 Heinemann, T. & Papaloizou, J. C. B. 2012, *MNRAS*, 419, 1085  
 Hirose, S., Krolik, J. H., & Stone, J. M. 2006, *ApJ*, 640, 901  
 Io, Y. & Suzuki, T. K. 2013, arXiv:1308.6427  
 Jiang, Y.-F., Stone, J. M., & Davis, S. W. 2013, *ApJ*, 778, 65  
 Johansen, A., Youdin, A., & Klahr, H. 2009, *ApJ*, 697, 1269  
 Käpylä, P. J. & Korpi, M. J. 2011, *MNRAS*, 413, 901  
 Krause, F. & Raedler, K.-H. 1980, *Mean-field magnetohydrodynamics and dynamo theory*  
 Kuncic, Z. & Bicknell, G. V. 2004, *ApJ*, 616, 669  
 Lesur, G., Ferreira, J., & Ogilvie, G. I. 2013, *A&A*, 550, A61  
 Lesur, G. & Longaretti, P.-Y. 2007, *MNRAS*, 378, 1471  
 Lesur, G. & Ogilvie, G. I. 2008, *MNRAS*, 391, 1437  
 Longaretti, P.-Y. & Lesur, G. 2010, *A&A*, 516, A51  
 Mignone, A., Bodo, G., Massaglia, S., Matsakos, T., Tesileanu, O., Zanni, C., & Ferrari, A. 2007, *ApJS*, 170, 228  
 Mignone, A., Flock, M., Stute, M., Kolb, S. M., & Musciani, G. 2012, *A&A*, 545, A152  
 Miller, K. A. & Stone, J. M. 2000, *ApJ*, 534, 398  
 Miyoshi, T. & Kusano, K. 2005, *J. Comput. Phys*, 208, 315  
 Noble, S. C., Krolik, J. H., & Hawley, J. F. 2010, *ApJ*, 711, 959  
 Ogilvie, G. I. 2003, *MNRAS*, 340, 969  
 Ogilvie, G. I. 2012, *MNRAS*, 423, 1318  
 Ohsuga, K. & Mineshige, S. 2011, *ApJ*, 736, 2  
 Oishi, J. S. & Mac Low, M.-M. 2011, *ApJ*, 740, 18  
 O'Neill, S. M., Reynolds, C. S., Miller, M. C., & Sorathia, K. A. 2011, *ApJ*, 736, 107  
 Paczyński, B. & Wiita, P. J. 1980, *A&A*, 88, 23  
 Parkin, E. R. & Bicknell, G. V. 2013a, *ApJ*, 763, 99  
 Parkin, E. R. & Bicknell, G. V. 2013b, *MNRAS*, 435, 2281  
 Pessah, M. E., Chan, C.-K., & Psaltis, D. 2006, *MNRAS*, 372, 183

- Rider, W. J., Greenough, J. A., & Kamm, J. R. 2007, *J. Comput. Phys*, 225, 1827
- Salvesen, G., Beckwith, K., Simon, J. B., O'Neill, S. M., & Begelman, M. C. 2013, arXiv:1303.5052
- Shakura, N. I. & Sunyaev, R. A. 1973, *A&A*, 24, 337
- Shi, J., Krolik, J. H., & Hirose, S. 2010, *ApJ*, 708, 1716
- Simon, J. B., Hawley, J. F., & Beckwith, K. 2009, *ApJ*, 690, 974
- Simon, J. B., Hawley, J. F., & Beckwith, K. 2011, *ApJ*, 730, 94
- Sorathia, K. A., Reynolds, C. S., & Armitage, P. J. 2010, *ApJ*, 712, 1241
- Sorathia, K. A., Reynolds, C. S., Stone, J. M., & Beckwith, K. 2012, *ApJ*, 749, 189
- Stone, J. M., Hawley, J. F., Gammie, C. F., & Balbus, S. A. 1996, *ApJ*, 463, 656
- Suzuki, T. K. & Inutsuka, S.-i. 2009, *ApJL*, 691, L49
- Suzuki, T. K. & Inutsuka, S.-i. 2013, arXiv:1309.6916
- Suzuki, T. K., Muto, T., & Inutsuka, S.-i. 2010, *ApJ*, 718, 1289
- Terquem, C. & Papaloizou, J. C. B. 1996, *MNRAS*, 279, 767
- Tout, C. A. & Pringle, J. E. 1992, *MNRAS*, 259, 604
- Turner, N. J., Stone, J. M., Krolik, J. H., & Sano, T. 2003, *ApJ*, 593, 992
- Uzdensky, D. A. 2013, *ApJ*, 775, 103
- Xu, K. & Li, Z. 2001, *International Journal for Numerical Methods in Fluids*, 37, 1